Global and Planetary Change 190 (2020) 103192

Contents lists available at ScienceDirect

Global and Planetary Change

journal homepage: www.elsevier.com/locate/gloplacha

Research Article

Water vapor variability in the Atacama Desert during the 20th century

Christoph Böhm*, Mark Reyers, Jan Herbert Schween, Susanne Crewell

Institute for Geophysics and Meteorology, University of Cologne, Cologne, Germany

ARTICLE INFO

Keywords:
Water cycle
Integrated water vapor
ERA-20C
Atacama
Hydrological cycle
Moisture transport

ABSTRACT

This study focuses on integrated water vapor (IWV) which is the main source for precipitation, fog and dew formation in the Atacama Desert in northern Chile. In order to study its long-term variability, a consistent meteorological record is needed. Here, we utilize the European Centre for Medium-Range Weather Forecasts' reanalysis ERA-20C which provides IWV among other atmospheric variables over the course of the entire 20th century (1900–2010). In this two fold study, we first present a validation of ERA-20C IWV for the Atacama and the bordering southeast Pacific region. Comparisons to satellite observations, i.e. the Hamburg Ocean Atmosphere Parameters and Fluxes from Satellite data record and the Moderate Resolution Imaging Spectroradiometer measurements, for overlapping time periods prove the suitability of ERA-20C to study IWV variability. Assessment of the observation feedback in ERA-20C reveals a higher uncertainty for the beginning of the 20th century when fewer observations are assimilated. Nevertheless, departures of the assimilated observations do not show a systematic bias in space or time supporting suitability of ERA-20C for long-term investigations. In the second part of the study, we describe the IWV variability over the course of the 20th century. Deviations from the long-term mean greater than 30% are found on an inter-annual time scale over the continental Atacama. Furthermore, we investigate potential drivers of the IWV variability such as the Pacific Decadal Oscillation (PDO) and the El Niño Southern Oscillation (ENSO) phenomenon. The relationship between the local IWV and these large scale indices depends on region and season. For instance, during austral summer, La Niña conditions yield overall greater IWV variability in the Atacama allowing both drier and even more pronounced wetter extremes than El Niño conditions.

1. Introduction

The Atacama Desert in northern Chile is one of the driest places on Earth. Nevertheless, it hosts a variety of species and microorganisms which adapted to the concurrent hyper-arid conditions. Their spatial appearance is not well understood but it is likely connected to the availability of water. For instance, Pinto et al. (2006) found that the geographical distribution of Tillandsia lomas is associated with fog corridors. Furthermore, events of extreme precipitation or wetter time periods on geological time scales can leave long lasting traces in the landscape and impact biological evolution and colonization. Characterizing the moisture supply to the Atacama Desert in the context of the recent climate is essential in order to establish thresholds for growth and development of the local biota and for surface alterations.

Water vapor, which amounts to about 99.5% of the total water in the atmosphere (Stevens and Bony, 2013), is the most important source for precipitation and is the key variable for fog formation and dew. Aside from these obvious sources of liquid water for plants and surfaces, water vapor itself constitutes a direct source of water for soils in arid regions via water vapor adsorption and thereby stimulating microbial activity (McHugh et al., 2015). Furthermore, relative humidity along with temperature determines the phase transitions between gypsum, anhydrite and their intermediate phases which has been demonstrated in theory by Tang et al. (2019). Relative humidity and the isotopic composition of the water vapor which is related to its source and pathway are essential variables in order to develop a paleo-humidity proxy (Surma et al., 2018). A better knowledge of the spatiotemporal distribution of water vapor over a longer time period could help improve the accuracy of such a proxy.

Another field of application for water vapor in the Atacama Desert is Astronomy. The region is home to multiple astronomical facilities, such as the European Southern Observatory (ESO) which operates for instance the Very Large Telescope at the summit of Cerro Paranal. Even though, the Atacama provides a hyper-arid environment, water vapor is still a limiting factor of atmospheric transparency in the millimeter and submillimeter wavelength spectral window. Characterizing the variability of water vapor and identifying potential drivers benefits the development of the observatories and planning the conduction of very

* Corresponding author.
E-mail address: c.boehm@uni-koeln.de (C. Böhm).

https://doi.org/10.1016/j.gloplacha.2020.103192
Received 31 May 2019; Received in revised form 20 December 2019; Accepted 13 April 2020
Available online 22 April 2020

demanding observations (Kerber et al., 2014; Otarola et al., 2019). Water vapor is one of the key factors which determine the surface solar radiation budget (Rondanelli et al., 2015). The higher elevated parts of the Atacama were found to be the most likely location with the highest downwelling solar radiation at the surface on Earth (Rondanelli et al., 2015). The extreme solar radiation also results in an extreme exposure of the surfaces to ultraviolet radiation (Cordero et al., 2016) which is a limiting factor to bacterial life (Cockell et al., 2008).

The influence of internal climate modes such as the El Niño Southern Oscillation (ENSO) pattern or the Pacific Decadal Oscillation (PDO) on precipitation and water vapor content has been assessed for the Atacama region and the bordering Altiplano in various studies (e.g. Garreaud, 1999; Vuille, 1999; Vargas et al., 2006; Houston, 2006; Garreaud et al., 2009; Marín and Barrett, 2017). For instance, through evaluation of gauge measurements it was demonstrated that the warm phase of ENSO (El Niño) leads to more precipitation at coastal stations and less precipitation in the Altiplano during austral summer (Houston, 2006). Furthermore, the PDO, which shows similar patterns in SST anomaly as ENSO but acts on a much longer time scale (Garreaud et al., 2009), appears to amplify the ENSO signal during its warm phase (Andreoli and Kayano, 2005). On a synoptic scale, cut-off lows over the adjacent southeast Pacific are associated with increased moisture supply to the Atacama Desert (e.g. Bozkurt et al., 2016; Reyers and Shao, 2019).

Water vapor is a major part of the water cycle being the dominant phase which is subject to transport. More details on the atmospheric water cycle in the Atacama region are given in Section 2.6. Due to the scarcity of in-situ measurements especially over longer time periods, region-wide studies on a climatological scale are limited. Satellite observations can provide greater spatial coverage but are temporally limited to the satellite era which started in the 1980s. For long term trend analyses and to study dependencies on low frequency internal climate modes such as the ENSO pattern or the PDO, longer time series are beneficial. Such time series with broad spatial and temporal resolution including multiple atmospheric parameters can only be provided by reanalyses data. Reanalyses combine model simulations and observations to obtain the best estimate of the true state of the atmosphere. To our knowledge four reanalyses data sets which cover the entire 20th century are available as of today, namely the National Oceanic and Atmospheric Administration's (NOAA) Twentieth Century Reanalysis (20CR) and its successor 20CRv2c (Compo et al., 2011) and the European Centre for Medium-Ranged Weather Forecasts (ECMWF) twentieth century reanalysis (ERA-20C Poli et al., 2016) and a later release with a coupled ocean model (CERA-20C Laloyaux et al., 2018). In this study, we utilize ERA-20C (see Section 2.1). The accuracy of reanalyses depends on the model representation of the physical processes and on parameter schemes for processes which happen at scales below the model resolution. Furthermore, the accuracy of the assimilated observations and the abundance of observations plays a role as well as the accuracy of the prescribed forcing data, e.g. sea ice concentration, sea surface temperature, aerosols, etc. Additionally, complex orography with large variability on scales not resolved by the model can decrease the accuracy. Therefore, the accuracy of a reanalysis typically varies in space and time, so that a validation for the particular study area and time period is inevitable to determine the suitability for an application.

Integrated water vapor (IWV) is the moisture related variable which can be observed most accurately from satellite measurements compared to liquid water path or precipitation as the latter show much higher spatiotemporal variability. Thus, due to its role as the major storage term in the atmospheric water cycle and its good measurability, we focus this study on IWV.

Here, we present a two fold study, which firstly investigates the capabilities of ERA-20C to represent IWV in the Atacama region and secondly provides an analyses of the 20th century IWV. The paper is structured as follows. In Section 2, we describe ERA-20C, and the satellite data products which are utilized for a comparison. Section 3 presents the validation of the reanalysis by comparing the different satellite products for four different regions. In Section 4, we discuss the spatiotemporal variability of the IWV over the entire time period of 111 years covered by ERA-20C and its relation to large scale indices such as ENSO and PDO. Finally, Section 5 concludes the study.

2. Data and focus regions

2.1. ERA-20C

The ECMWF reanalysis ERA-20C (Poli et al., 2016) provides a consistent meteorological record spanning 111 years (1900–2010) with a horizontal resolution of about 125 km. Therefore, for this study area, data on a $1.25^\circ \times 1.25^\circ$ longitude by latitude grid are investigated. It is based on ECMWF's weather forecasting system IFS cy38r1 and run with time varying prescribed forcing data such as sea ice concentration, sea surface temperature (SST), solar radiation, tropospheric and stratospheric aerosols, ozone and greenhouse gases. To approximate the concurrent synoptic conditions, the assimilation of surface pressure and marine surface wind are essential. To avoid introducing break points and trends in the representation of the atmosphere, observations which are only available for more recent years, such as vertical profiles and satellite observations, were left out. Atmospheric reanalyses typically assimilate vertical humidity profiles from radiosonde data. Humidity from radiosondes is usually not homogenized, so that artificial trends of water vapor can be introduced into these reanalyses (Dai et al., 2011) among other complications (Elliott and Gaffen, 1991). Since ERA-20C does not consider radiosonde data, it is not affected by any of such inhomogeneities.

Poli et al. (2016) compared integrated water vapor (IWV) spatially averaged over the tropical oceans (20°S–20°N) from ERA-20C to two observational products, i.e. the Remote Sensing Systems version 7 IWV product (RSS; Wentz (2013)) and the Hamburg Ocean Atmosphere Parameters and Fluxes from Satellite data record version 3.2 (HOAPS; Fennig et al. (2012)). Their resulting time series reveal a dry bias of ERA-20C of approximately 2–3 $\mathrm{kg\,m^{-2}}$. However, when anomalies with respect to a long term mean are considered, ERA-20C IWV agrees better with the observations than the Japanese 55-year Reanalysis (JRA-55) and the widely used ERA-Interim from ECMWF. Therefore, it seems well suited for the analysis of climate variability.

2.2. HOAPS4

In order to validate IWV values in ERA-20C, we utilize IWV estimates from the most recent version 4 of the Hamburg Ocean Atmosphere Parameters and Fluxes from Satellite data record (HOAPS; Andersson et al. (2017a)). This data record provides satellite based retrievals of IWV as 6-hourly composites on a $0.5^\circ \times 0.5^\circ$ longitude by latitude grid for the period between July 1987 to December 2014. The retrievals are derived from Special Sensor Microwave/Imager (SSM/I, Hollinger et al., 1990) measurements. They are only provided over ice free ocean where the microwave emission by water vapor can be separated well from the surface signal. By utilizing radiation in the microwave spectrum, retrievals are possible for all sky conditions except for heavy precipitation which can lead to strong scattering.

Generally, SSM/I based data records, such as HOAPS, provide IWV retrievals of similar quality regarding stability and homogeneity whereas non-SSM/I data records contain relatively large break points which coincide with changes in the observational set up. This can lead to different trend estimates from such records which are not in line with theoretical expectations (Schröder et al., 2016; Andersson et al. 2017b).

2.3. MODIS

To allow an evaluation of ERA-20C IWV over land, we further utilize

IWV retrievals from the Moderate Resolution Imaging Spectroradiometer (MODIS) which is installed aboard the Terra satellite and the Aqua satellite. The MOD05_L2 (on Terra; Borbas et al., 2017a) and the MYD05_L2 (on Aqua; Borbas et al., 2017b) products provide IWV retrievals which are derived from near infrared (NIR) and infrared (IR) channels for both satellites at 1 km (NIR) and 5 km (IR) horizontal resolution. Here, we utilize collection 6.1 which is the newest MODIS collection. We only use the near infrared retrievals because they show higher accuracy than the infrared retrievals (Steinke et al., 2015). These are available for surfaces which are highly reflective in the near infrared such as clear land areas, clear ocean areas with sun glint, or clouds above ocean or land. However, if the reflector is a cloud, the retrieved IWV is not representative of the entire atmospheric column because the water vapor path between the surface and the cloud is not fully captured. For the calculation of spatial means of the MODIS IWV, we omit scenes for which the reflector type is a cloud according to the MODIS water vapor product. A potential "clear sky" bias is assumed to be negligible considering the reflector type is a cloud for only 7 % out of of all retrievals for the inland regions.

MODIS retrievals are available from February 2000 (Terra) and from July 2002 (Aqua) to present. For the climatology study (Section 3.2), we only utilize Terra MODIS to benefit from the longer data record. The 10-year period between 2001 and 2010 is considered. For the analysis of the variability over time (Section 3.4), we consider the 8-year period between 2003 and 2010 to benefit from additional Aqua MODIS retrievals. The equatorial overpass time of the satellites are around 10:30 (Terra) and 13:30 (Aqua) local solar time. The uncertainty for MODIS IWV retrievals typically ranges between 5% and 10% (Gao and Kaufman, 2003). A previous study revealed a spatially varying dry bias between 1.6 and 3.5 mm of the MODIS NIR IWV compared to GPS derived IWV within the Atacama region (Remy et al., 2011). Furthermore, the authors report good agreement of the IWV variability (1.3 mm standard deviation between GPS and MODIS retrievals after a linear correction). A more recent study carried out over North America reveals a wet bias of the MODIS NIR water vapor product of 4.1 mm, an RMSE of 5.6 mm and coefficient of determination of 0.964 over land (He and Liu, 2019). Another study in a drier continental environment (Iran) revealed a wet bias of 2.4 mm, an RMSE of 3.4 mm and a correlation coefficient of 0.95 (Khaniani et al., 2020). Both of these studies used Global Positioning System IWV retrievals as reference and considered a one year period for their comparisons. Judging from these studies, the bias seems to depend on the study area. However, suitable representation of IWV variability is proven by all of these comparisons.

2.4. Large scale indices ENSO and PDO

The ENSO pattern is a variability in the climate system manifested in alternating cold and warm phases in the surface temperature of the eastern tropical pacific which has strong influence on weather all over the globe (e.g. Timmermann et al., 2018). During the warm phase (El Niño), above average sea surface temperatures close to the western coast of South America lead to locally decreased stability of the troposphere and changes of the large scale circulation. For instance, enhanced upper tropospheric westerlies due to a northward displacement of the Bolivian High lead to drier conditions in the Altiplano (Vuille, 1999). On the other hand, during the cold phase (La Niña) enhanced tropospheric stability over the southeast Pacific favors drier conditions at the southern coast of the Atacama (Houston, 2006). To quantify the ENSO state, various indices have been created. Here, we apply the commonly used Niño 3.4 index which represents the SST anomaly of the equatorial Pacific between 5°S–5°N and between 170°W–120°W. To calculate this index, we obtained SST data from https://www.esrl.noaa.gov/psd/gcos_wgsp/Timeseries/Data/nino34.long.data (last access: 20 May 2019) which provides spatially averaged SST values for the Niño 3.4 region with a monthly resolution. These data are sampled from the Met Office Hadley Centre's sea ice and sea surface temperature data set, HadISST1 (Rayner et al., 2003). The HadISST1 provides a long continuous SST time series (1870–present). To derive the Niño 3.4 index, we calculate the monthly SST anomalies. Only the years of our study period, which is determined by ERA-20C (1900–2010), are considered. The two different versions of HadISST for ERA-20C (Version 2.1) and the Niño 3.4 index (Version 1) are highly correlated ($r = 0.96$). Therefore, no noticeable implications on the analysis are expected.

In contrast to ENSO, which is focused on the equatorial Pacific, the PDO represents a major climate variability pattern centered over the midlatitude North Pacific basin. It has been defined as the principle component of the leading Empirical Orthogonal Function (EOF) of the SST anomalies (e.g. Mantua et al., 1997; Zhang et al., 1997) for the Pacific north of 20°N. Here, we apply the PDO index according to Mantua et al. (1997) which is based on the U.K. Meteorological Office Historical Sea Surface Temperature data set (Folland and Parker 1990, 1995) for the years between 1900 and 1981 and on the Reynold's Optimally Interpolated SST from 1982 to present. The PDO index was downloaded from http://research.jisao.washington.edu/pdo/PDO.latest.

Furthermore, local SST anomalies which are determined from the ERA-20C SST as a spatial mean between 18.125°S–29.375°S and 75.625°W–71.875°W on a monthly resolution are considered as local SST "index". The chosen region lies in close proximity to the coast off the Atacama (black rectangle in Fig. 1b).

2.5. Cut-off lows

To evaluate the capabilities of ERA-20C to represent synoptic features which potentially impact IWV variability, we consider cut-off lows off the coast of the Atacama (Section 3.2). Therefore, we utilize the cut-off low data set derived by Reyers and Shao (2019). They define cut-off lows as a local minimum of the geopotential height in 500 hPa within the area ranging from 85°W to 70°W and from 30°S to 15°S (black rectangle in Fig. 2 c, f, i). Geopotential heights were taken from the ECMWF reanalysis ERA-Interim (Dee et al., 2011). To derive a list of days which featured a cut-off low, the 12 UTC ERA-Interim output was considered. More details on cut-off lows in the Atacama can be found in Reyers and Shao (2019).

2.6. Focus regions and local atmospheric water cycle

A simplified water cycle for the Atacama region is depicted in Fig. 1. The maritime boundary layer (MBL) is fueled with moisture by evaporation from the Pacific. Turbulent mixing results in a vertically almost constant specific humidity within the MBL which has an average height between 800 and 1100 m (Rutllant et al., 2003; Muñoz et al., 2011). Adiabatic cooling with increasing height causes the water vapor to reach saturation, so that condensation leads to cloud formation. Due to the location at the subsiding end of the Hadley circulation, the MBL is topped by a strong temperature inversion which prevents the exchange between the MBL and the free troposphere above. Therefore, the cloud top height is limited to the base height of the temperature inversion. Longwave radiative cooling at cloud top maintains the stratocumulus or leads to further expansion. During the day, the surface at the coast and coastal cliff warm more than the ocean water leading to ascending motion at the cliff. This drives a circulation with a flow towards the coast above the surface and a return flow beneath the inversion base height, causing the stratocumulus cloud to be advected away from the coast. At night, though less pronounced, the circulation is reversed. Along with an even more effective radiative cooling, the strocumulus cloud deck can then penetrate the coastal cliff area. Even stronger heating of the Andean slopes during the day creates a strong inland flow above the coastal cliff which end in an upward motion in the high Andes creating convective clouds and precipitation. A return flow at higher altitudes leads to increased subsidence over the ocean

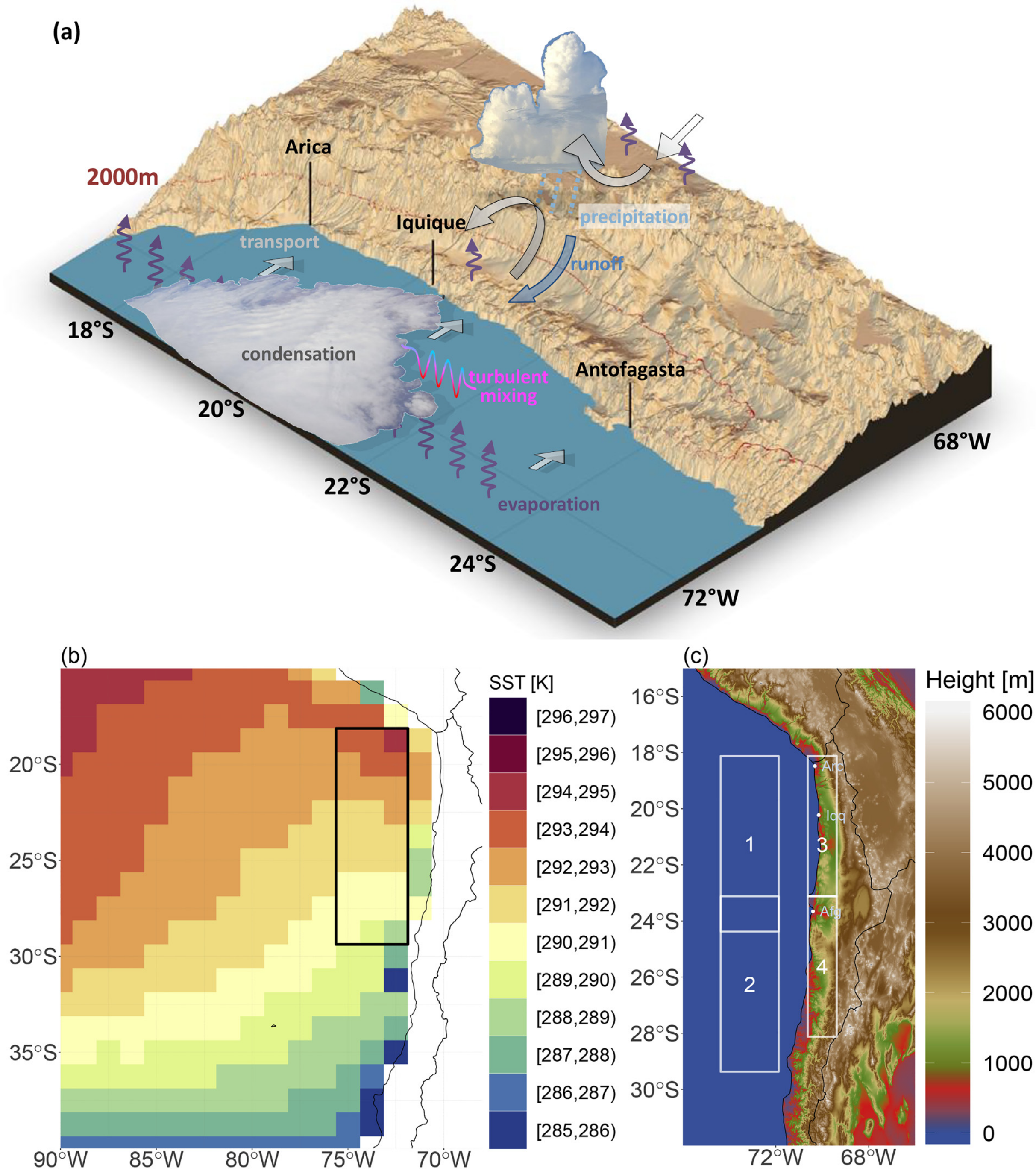

Fig. 1. (a) Schematic depiction of the simplified atmospheric water cycle for northern Chile and its surrounding area. Over land, day time conditions are reflected. Strong heating of the Andean slopes leads to a rising branch of the flow in the high Andes and a return flow at around 5000 m which causes additional subsidence above the coastal region. Below this upper circulation cell, another circulation cell typically establishes in the maritime boundary layer. Here, early night time condition are depicted. A stronger cooling of the coastal cliff compared to the ocean surface causes a weak flow towards the coast so that the stratocumulus clouds can spread towards the cliff and penetrate the coastal mountain range. (b) Mean ERA-20C SST averaged between 1900 and 2010. (c) Topography derived from the Shuttle Radar Topography mission (SRTM) data set. The white rectangles denote the four focus regions which are studied. Their sizes are given by the size and position of the ERA-20C grid boxes (1.25 $^{\circ}$ $\times$ 1.25°). Regions 1 (ocean-N) and 2 (ocean-S) span 5 $\times$ 2 grid boxes, regions 3 (land-N) and 4 (land-S) span 4 $\times$ 1 grid boxes.

and coastal area. Therefore, two circulation cells are established (Rutllant et al., 2003). In case the top of the coastal cliff, which has altitudes ranging between 400 and 1500 m, is below the inversion base height, the MBL cell and the cell atop are coupled and Pacific moisture can be transported inland. When the stratocumulus is advected inland the mixing with warmer and drier inland air leads to dissipation of the cloud. However, the air with enhanced water vapor can still be transported further inland where night time cooling might lead to the formation of radiation fog (Cereceda et al., 2002).

The inland regions are characterized by fog at the coastal cliff and coastal cordillera which typically forms at night and dissipates during the morning hours after sunrise (Cereceda et al., 2008). Further inland, clouds are rarely observed. Due to these differences, we distinguish between inland and ocean for the validation. Furthermore, inland precipitation decreases from south to north in particular during winter season (Houston, 2006) which indicates the influence of the

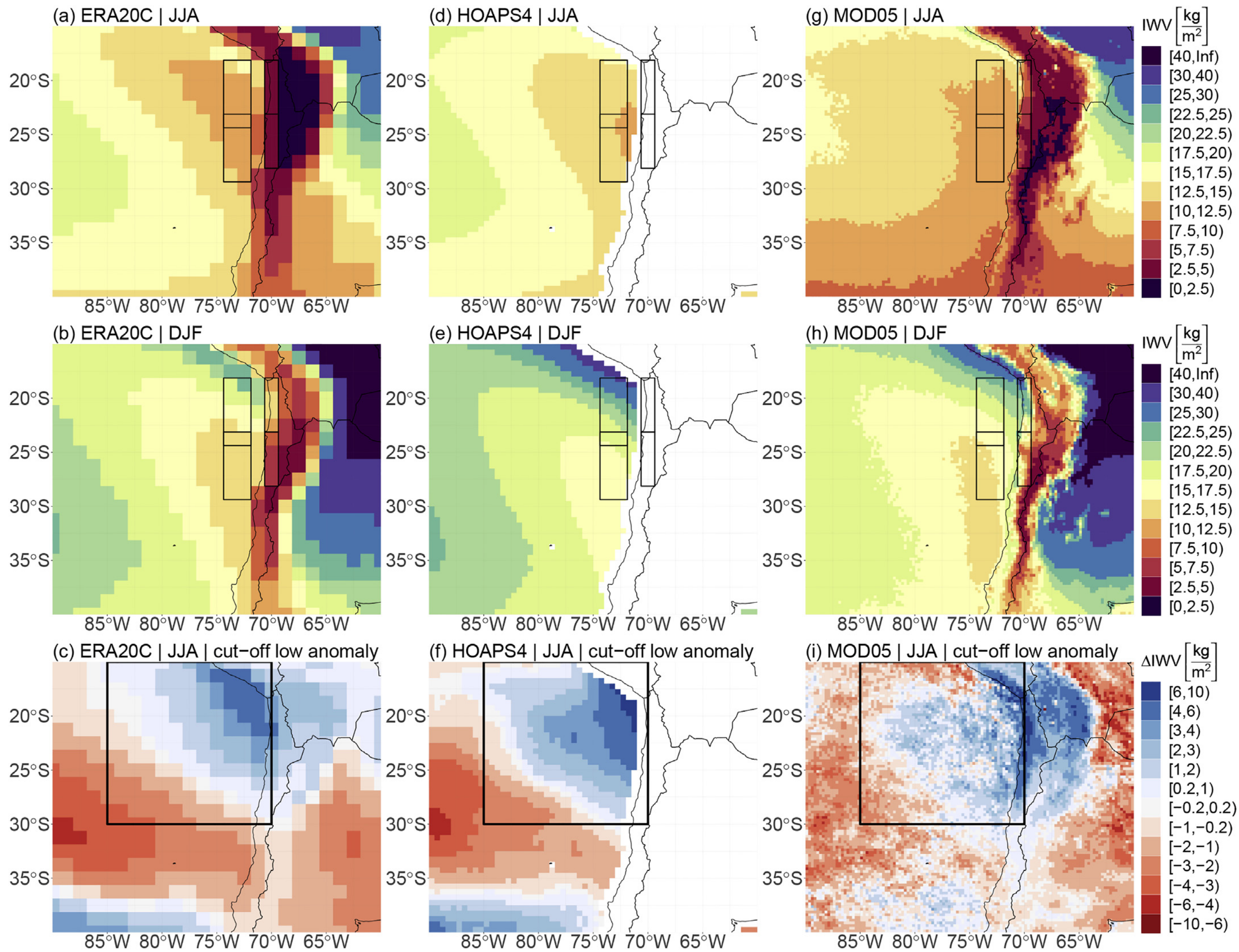

Fig. 2. Composite means of IWV retrieved from ERA-20C (a,b,c), HOAPS (d,e,f) and Terra-MODIS (g,h,i) for winter season (JJA, top row), summer season (DJF, middle row) and composite anomalies of IWV for days for which the presence of a cut-off low was identified in ERA-Interim (bottom row). Here, cut-off lows are defined as a local minimum of the geopotential height in 500 hPa (Reyers and Shao, 2019) within the region from 85°W to 70°W and 30°S to 15°S which is denoted by the black rectangle (c,f,i). Composites are taken for a 10-year period (2001–2010).

midlatitude storm tracks in the southern part. The stronger influence of frontal systems in the southern part calls for an additional distinction in northern and southern regions. Therefore, we focus on four individual regions (Fig. 1). Region 1 (18.125°S–24.375°S) and 2 (23.125°S–29.375°S) are over ocean (74.375°W–71.875°W), and region 3 (18.125°S–23.125°S) and 4 (23.125°S–28.125°S) are mainly over land (70.625°W–69.375°W).

3. Validation of ERA20C

To estimate how well IWV is represented in ERA-20C, we carry out a comparison with HOAPS and MODIS IWV. By choosing the Terra-MODIS IWV, a 10-year period (2001 – 2010) with retrievals from all three data sets can be compared. Average IWV values for each data record and each of the defined focus region are given in Table 1 revealing a dry bias of ERA-20C between 18% (north) and 14% (south) for the ocean regions (compared to HOAPS) and between 45% (north) and 46% (south) for the inland regions (compared to Terra-MODIS). Potential origins of this bias are discussed in Section 3.1. Henceforward, spatial patterns are discussed for composites and seasonal means of the IWV (Section 3.2) followed by an analysis of decomposed IWV time series (Section 3.3). The representativity of the validation, which is

Table 1
10-year (2001–2010) mean IWV values for the focus regions indicated in Fig. 1 for all months, austral winter months, i.e. June, July, August (JJA), and austral summer months, i.e. December, January, February (DJF). Values are given in kg m^{-2}.

	Season	Ocean		Inland	
		North	South	North	South
HOAPS	All	17.46	14.65		
	JJA	13.38	12.91		
	DJF	22.21	16.95		
Terra MODIS	All	15.99	12.96	14.68	8.90
	JJA	12.26	11.63	9.23	5.66
	DJF	18.57	15.17	20.87	12.90
Terra MODIS land only	All			13.9	8.5
	JJA			7.1	5.2
	DJF			20.8	12.2
ERA-20C	All	14.33	12.55	8.13	4.83
	JJA	12.00	11.77	4.52	3.75
	DJF	17.15	13.78	12.91	6.60

carried out for recent decades, for the entire period covered by ERA-20C is discussed in Section 3.4.

3.1. Bias assessment

Since a substantial bias between the satellite data sets and ERA-20C is evident from the climatologies (Table 1), we investigate whether the reasons of this bias potentially hamper ERA-20C's suitability for the assessment of long term IWV variability within the study region. Several factors can contribute to the bias, e.g. instrumental factors, omitting cloudy scenes for the MODIS NIR retrievals, or problems inherent to the reanalysis.

Starting with the ocean regions, we approximate the expected IWV by the following conceptual considerations. Assuming a well mixed boundary layer with a vertically constant specific humidity and a negligible water vapor content within the free troposphere aloft, the IWV is only a function of SST and the inversion height. The specific humidity is approximated, assuming a relative humidity of 80% at the surface. According to ERA-20C, the mean SST for the northern ocean region is approximately 22°C and 17°C for the summer and winter season, respectively. According to vertical profiles acquired by radio soundings near Antofagasta (70.4°W; 23.4°S), the inversion base height ranges between 900 m (winter) and 1100 m (summer) (Muñoz et al., 2011). Towards the northwest, the inversion base height is increasing (Rahn and Garreaud, 2010), so that inversion base heights about 100–200 m above the heights at Antofagasta appear realistic. Such SSTs and inversion base heights amount to theoretical IWV values of 20 and 12 $kg\,m^{-2}$ for summer and winter season, respectively (cf. Fig. S1). Considering the coarse resolution of the utilized SST which might cause an underestimation of the strong SST gradient at the northern tip of the focus region and a missed component of the free troposphere, these theoretical values constitute a lower bound of the expected IWV. In this light, the slightly higher HOAPS IWV appears realistic while ERA-20C underestimates the IWV.

Judging from the ERA-20C temperature profiles within the lower troposphere, an underestimation of the inversion height of about 50% is revealed compared to results from the Variability of the American Monsoon Systems Ocean-Cloud-Atmosphere-LandStudy Regional Experiment (VOCALS-REx; Wood et al., 2011; Rahn and Garreaud, 2010) (cf. Fig. S1a). Such underestimations near the coast of subtropical stratocumulus regions are typical for numerical models (Rahn and Garreaud, 2010; Hannay et al., 2009; Wyant et al., 2010). For an inversion height of about 600 m, the theoretical boundary layer contribution to the IWV amounts to about 7 and 10 $kg\,m^{-2}$ for winter and summer season, respectively (cf. Fig. S1). Furthermore, for the time period in the case study, about 20% of the total IWV are contributions from height levels between the modeled and the observed inversion base height, partially compensating for the missing moisture below the inversion base. Therefore, we conclude that the dry bias originates from an underestimation of the inversion base and a false representation of the vertical humidity profile within the boundary layer.

For the two inland regions, we investigate the bias between ERA-20C and the MODIS near-infrared retrievals. While Remy et al. (2011) reveal a dry bias of the MODIS NIR IWV, ERA-20C shows even lower values in our study. This bias can be partially attributed to the coarse height representation in ERA-20C (Fig. S2). The average height of the northern inland region is about 1297 m in ERA-20C which is about 342 m above the height according to Shuttle Radar Topography Mission (SRTM; Farr et al., 2007) data (955 m). For the southern inland region the overestimation is about 191 m (ERA-20C: 1778 m; SRTM: 1587 m). An approximation of specific humidity of 4 $g\,kg^{-1}$ (JJA) and 9 $g\,kg^{-1}$ (DJF) yield a theoretical difference in IWV of 1.5 $kg\,m^{-2}$ (JJA) and 3.3 $kg\,m^{-2}$ (DJF) for the northern region and 0.8 $kg\,m^{-2}$ (JJA) and 1.8 $kg\,m^{-2}$ (DJF) for the southern region. However, in particular for the northern region a higher bias is expected because the northern tip of the region has an actual even lower altitude allowing the penetration of moist air from the MBL inland more frequently which is manifested in a higher fog and low cloud occurrence in this region. This contribution to the region wide mean IWV is not represented in ERA-20C due to its coarse resolution. The same holds true for coastal strips and valleys such as the Rio Loa valley which are not represented in ERA−20C.

According to the performed case study including theoretical considerations, the bias between ERA-20C and the satellite-based IWV can be attributed mainly to the reanalysis. The reasons are a false representation of the MBL (ocean) and topography (inland). Both effects constitute systematic errors and thus should not interfere with the representation of temporal variability. Composite IWV anomalies for cut-off low situations show similar magnitudes and spatial patterns for both ERA-20C and the satellite-based data sets, demonstrating the ability to capture IWV variations on a synoptic scale (Section 3.2).

3.2. Climatologies and composites

Across a wider area, the seasonal means over this 10-year period reveal a meridional pattern over ocean with higher IWV to the west and lower IWV closer to the coast for all three data sets (Fig. 2). This can be attributed to the lower SST in closer proximity to the coast where the Humboldt current is strongest (Fig. 1). During the summer season, i.e. December, January, February (DJF), IWV observed by all three data sets is higher than during winter season, i.e. June, July August (JJA) (Table 1). While HOAPS shows an increase from winter to summer of about 66% and 31% for the northern and southern regions, respectively, the increase in ERA-20C is about 43% and 17%, respectively. Again, a higher SST causes enhanced evaporation so that IWV increases in particular over ocean. The southeast Pacific anticyclone typically shifts towards the south in the summer season causing the surface winds which drive the Humboldt current to shift south as well. This way, the SST reaches maximum values in particular ahead of the Peruvian coast (15°S–20°S). Enhanced IWV is found for this region in all three data sets. Aside from higher SSTs, the summer season is also characterized by higher air temperatures providing a higher water vapor holding capacity and advection of already water vapor enriched air. Accordingly, MODIS and ERA-20C show an increased IWV over land during the summer season. Between 20°S–26°S, cloud heights are typically higher during the warm season (Böhm et al., 2019) which indicates a higher inversion base height. This could enable more Pacific moisture to cross the coastal cliff and be transported further inland leading to increased IWV in this region. On the eastern side of the Andes, a zonal pattern is revealed by ERA-20C and MODIS IWV with maximum values over the Amazon Basin and decreasing values towards the midlatitudes. Overall, ERA-20C is able to represent the patterns and seasonal changes which are observed by the satellite based data sets.

Furthermore, we investigated the influence of cut-off lows on the spatial distribution of IWV. Reyers and Shao (2019) found a higher moisture availability in the Atacama coinciding with these synoptic features. In this study, composite anomalies for cut-off low situations during the winter season show an enhanced IWV for the Atacama and for an extended area over the ocean off the Atacama coast (Fig. 2 c, f, i). In addition to the previously discussed agreement between the IWV patterns on a climatological scale, ERA-20C is even capable of representing the pattern of enhanced IWV for these synoptic features.

3.3. Comparison of decomposed IWV time series

To obtain time series for each data record, we calculate spatial and monthly means for each of the four focus regions. In order to evaluate the ability of ERA-20C to represent the IWV variability, we investigate the IWV deviation from the respective temporal mean of each time series. Furthermore, we decompose the time series into a 12-month centered moving average (CMA) a seasonal component and the residual. The seasonal component is derived by subtracting the 12-month CMA from the time series and then calculating the mean value for each

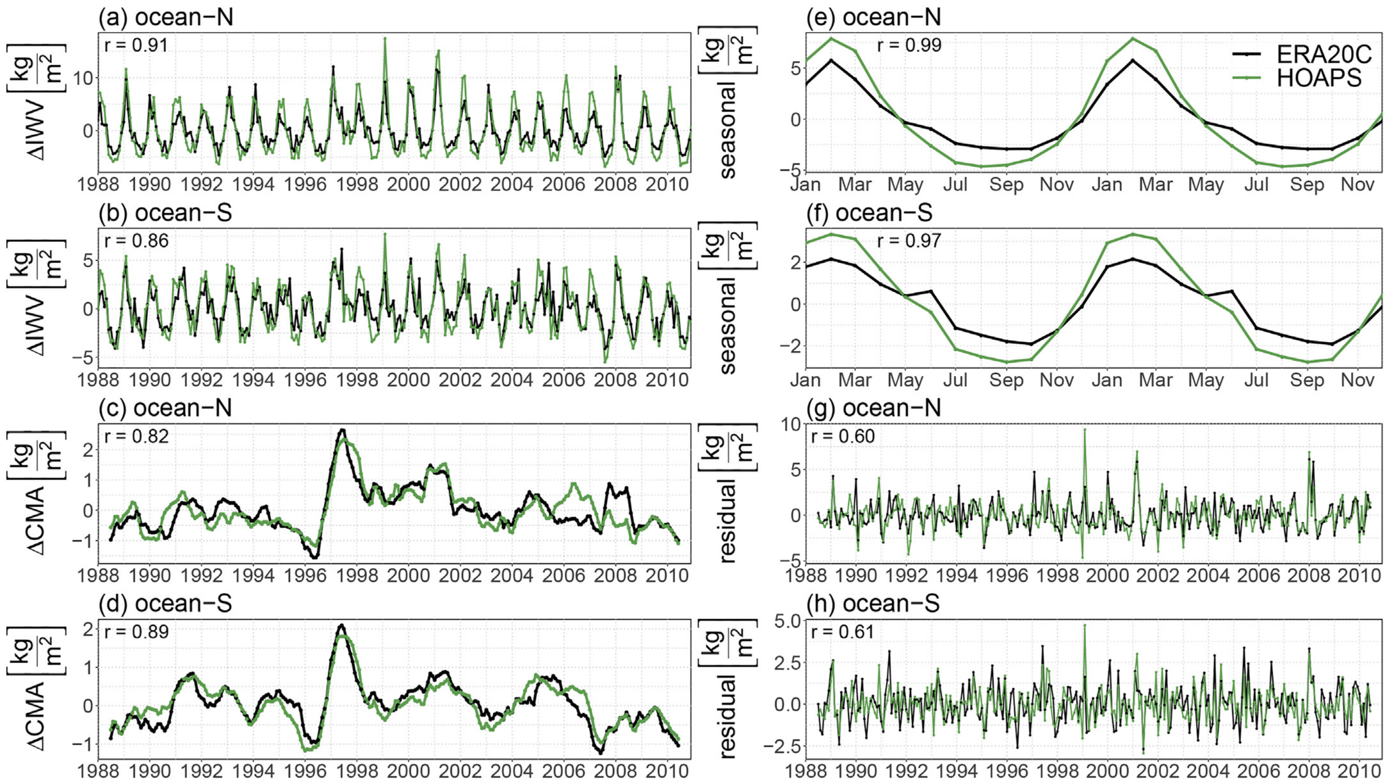

Fig. 3. IWV time series of ERA-20C and HOAPS for focus regions 1 and 2 (over ocean, denoted in Fig. 1). (a,b) Deviations from the respective means. (c,d) 12 months centered moving average of the ΔIWV time series. (e,f) seasonal cycle. (g,h) residuals. Correlation coefficients *r* are denoted at the top left of each panel. By adding the centered moving average, the seasonal cycle and the residual together, the overall time series of the deviation of the IWV results.

month. Subtracting the 12-month CMA and the seasonal component from the time series yields the residuals. While the 12-month CMA represents the year to year variability, the residuals are a measure of the month to month variability.

The unfiltered monthly time series of IWV for ERA-20C and HOAPS between 1988 and 2010 are highly correlated due to a consistent representation of the annual cycle and year to year variability (1-year CMA) for both the northern and the southern ocean regions (Fig. 3). The month to month variability (residuals) yield slightly lower correlations. A reason could be that synoptic features which pass through the regions might be slightly offset in time and space. The strong 1997 El Niño event is apparent in both data sets similarly. Only a small period (2005–2008) of ongoing disagreement between HOAPS and ERA-20C is apparent for the northern ocean region (1-year CMA, Fig. 3c).

The short period of disagreement and offset of the CMA between 2005 and 2008 within the northern region becomes a more dominant feature for the comparison between ERA-20C and MODIS IWV because the overlapping time period is much shorter (2003 − 2010). A missed peak during 2006 is followed by an offset period between 2007 and 2008 which is apparent in the 1-year CMA for both the northern ocean and inland region (Fig. 4). Before and after this period, ERA-20C IWV is in agreement with HOAPS and MODIS regarding both amplitude and phase. However, this short period of disagreement which is less pronounced for the southern regions results in overall low correlations of the 1-year CMA (Fig. 5 c, d). The month to month variability (residual) shows similar agreement between ERA-20C and MODIS (Fig. 5 e, f) as for the comparison between ERA-20C and HOAPS for the longer period. This indicates that ERA-20C is able to represent synoptic features although a substantial noise is present. This is expected given the coarse resolution of the model.

The phase of the seasonal cycle is captured accurately by ERA-20C which is indicated by correlations reaching almost unity for all regions (Fig. 5 a, b). The amplitude of the seasonal cycle is underestimated by ERA-20C, when absolute numbers are considered (Table 2). However, relative to its overall mean, the amplitudes are closer to the satellite-based estimates. These discrepancies are consistent with the detected misrepresentation of the maritime boundary layer (ocean) and topographic heights (inland) which result in an overall dry bias of the ERA-20C IWV (see Section 3.1).

The seasonal cycle is the main driver of variability according to the amplitudes (Table 2). Differences between summer and winter peaks range between 7.0 $kg\,m^{-2}$ (HOAPS, southern ocean region) and 12.9 $kg\,m^{-2}$ (HOAPS, northern ocean region). The month to month variability (residuals) superimposes another 5 $kg\,m^{-2}$ (north) and 3 $kg\,m^{-2}$ (south) of variability over ocean according to the difference between most upper and most lower peaks (c.f. Fig. 3, g, h). Similar values are observed for the inland regions with about 4 $kg\,m^{-2}$ (north) and 3 $kg\,m^{-2}$ (south).

A measure of uncertainty of the IWV representation in ERA-20C can be derived by calculating the root mean square error (RMSE) for the 3 components (seasonal cycle, moving average and residuals) of the IWV anomalies (Fig. 6). For the moving average, the RMSE between HOAPS and ERA-20C is about 0.56 $kg\,m^{-2}$ and 0.25 $kg\,m^{-2}$ for the northern and southern ocean regions, respectively. In relation to the long term mean values (Table 1) these values range around 3% and 2%. For the residuals, the RMSE between HOAPS and ERA-20C is about 1.09 $kg\,m^{-2}$ and 0.80 $kg\,m^{-2}$ for the northern and southern ocean regions, respectively. In relation to the long term mean values (Table 1) these values range around 6% and 5%.

An extension of the analysis beyond the four focus regions to a wider area reveals that the RMSE values are highest in the northern part of the study area where the variability is found to be highest (Fig. 7 e, f, g, h for ERA-20C against HOAPS and Fig. 8 e, f, g, h for ERA-20C against Terra-MODIS). While higher correlations regarding to the moving averages and the residuals are revealed in the south, higher correlations regarding to the seasonal cycles are revealed in the north

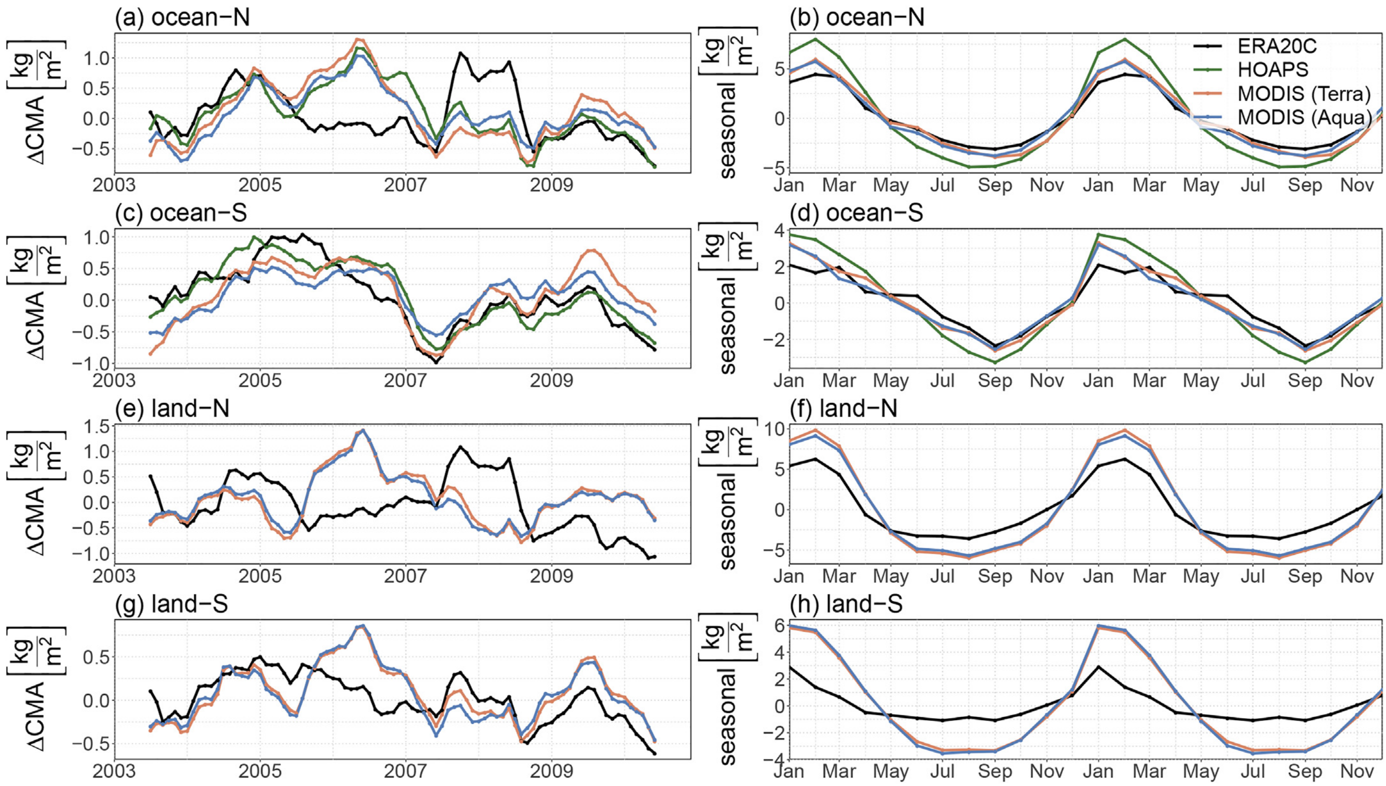

Fig. 4. IWV time series of ERA-20C, HOAPS, Terra-MODIS and Aqua-MODIS for region 1 (a,b), region 2 (c,d), region 3 (e,f), and region 4 (g,h) which are indicated in Fig. 1. Shown are the 1-year centered moving average (CMA) of the IWV anomalies (left) and the seasonal components (right). (For interpretation of the references to colour in this figure legend, the reader is referred to the web version of this article.)

(Fig. 7 a, b, c, d and Fig. 8 a, b, c, d).

3.4. Representativity for the 20th century

Thus far, the validation is carried out for a time period for which satellite-based IWV retrievals are available. To further assess how representative the validation is for the whole time period, we analyze the observations which were assimilated into ERA-20C. We utilize the number of assimilated surface pressure and marine surface wind observations along with their individual departures from the analyses after their assimilation. These data are provided by the ECMWF observation feedback archive (Hersbach et al., 2015). We consider any

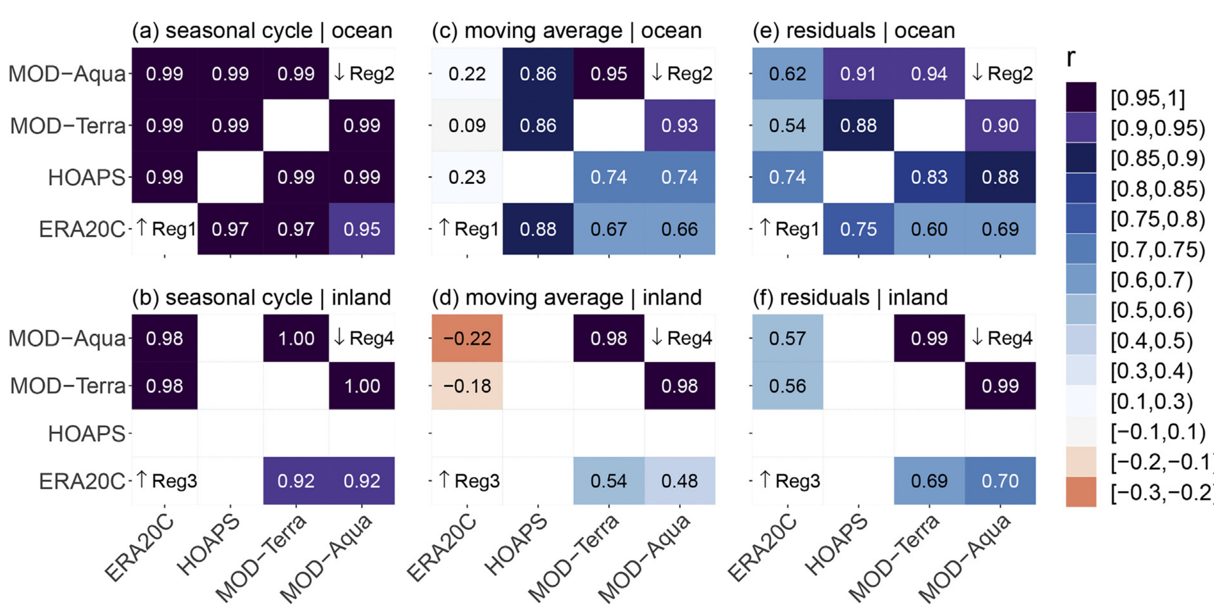

Fig. 5. Correlation of the decomposed time series of IWV between the different sources: Aqua MODIS NIR (MOD-Aqua), Terra MODIS NIR (MOD-Terra), HOAPS, and ERA-20C. (a,b) correlation of the seasonal cycle. (c,d) correlation of the centered moving average. (e,f) correlation of the residuals. Regions 1 and 2 (a,c,e) and 3 and 4 (b,d,f) are distinguished by showing the northern region in the upper left corner and the southern region in the lower right corner of each panel as indicated. The underlying time series comprise 8 years (2003–2010). Note that HOAPS is only available over ocean. (For interpretation of the references to colour in this figure legend, the reader is referred to the web version of this article.)

Table 2
Assessment of the seasonal cycles for the focus regions indicated in Fig. 1. Differences between summer and winter peaks $P_S - P_W$ for the seasonal cycles shown in Fig. 4 and long term mean IWV w (c.f. Table 1) are given in kg m^{-2}. The ratio between half of the peak difference and the long term mean IWV is given in percent.

	Data	Ocean		Inland	
		North	South	North	South
$P_S - P_W$	ERA-20C	7.6	4.4	9.8	4.0
	HOAPS	12.9	7.0		
	Terra MODIS			15.8	9.1
mean IWV w	ERA-20C	14.33	12.55	8.13	4.83
	HOAPS	17.46	14.65		
	Terra MODIS			14.68	8.90
$\frac{\frac{1}{2}(P_S - P_W)}{w}$ [%]	ERA-20C	26.5	17.5	60.3	41.4
	HOAPS	36.9	23.9		
	Terra MODIS			53.8	51.1

assimilated observations that are located within the region bounded by 90°W to 60°W and 40°S to 15°S. The total number of assimilated observations per year stayed below 5000 prior to the late 1950s except for a local maximum around 1910 (Fig. S3a). During the 1970s this number increased by a factor of greater than 25. The enormous increase is mainly due to additional observations over land (Fig. S3b). On a global scale, the number of assimilated observations increased continuously despite a few interruptions (e.g. after World War II) (Poli et al., 2016). Concurrently, the mean bias between ERA-20C and the assimilated observations decreased to almost zero by the late 1990s (Fig. S3b). The bias corrected mean absolute error decreased from about 1 hPa to at the beginning of the modeled period to about 0.5 hPa at the end of the period (Fig. S3b). This is not surprising, considering a denser observation network can add more realism to the model. This means, the uncertainties are higher for the earlier part of the time series, in particular prior to 1935. However, the spatio-temporal variability of the bias does not reveal any systematic pattern in space or time (Fig. S5). Therefore, there is no indication that the circulation pattern could be systematically offset for the earlier part of the 20th century.

As of today, no data with higher resolution than ERA-20C is available to study IWV for the entire 20th century. Overall, ERA-20C reveals a dry bias which has been shown already by Poli et al. (2016). However, the spatial distribution patterns agree well with satellite observations. Agreement of anomaly patterns for cut-off low situations even prove a good representation on a synoptic scale. The phase of the seasonal cycle is represented very accurately, even though the amplitude is underestimated. Year to year variability is found to be represented very well. However, a short time period was identified for which the moving averages of ΔIWV from ERA-20C diverged from the satellite based retrievals. Even for this period, the month to month variability is still in rather good agreement. Therefore, we conclude that ERA-20C represents the IWV variability sufficiently well for the Atacama and the bordering southeast Pacific region so that it can be utilized to study the IWV within this region over the course of the 20th century.

4. 20th century IWV

To investigate the long term IWV variability in the Atacama Desert, we consider the IWV deviations from the respective mean values for the entire period which is covered by ERA-20C (1900–2010) with a monthly resolution. First, the inter-annual to inter-decadal variability is discussed for the focus regions. Second, the relationships between the observed variability of IWV and the PDO, ENSO and local SST are investigated. Third, a seasonal distinction is shown.

4.1. Regional IWV variability

The 1-year, 5-year, and 10-year centered moving averages (CMA) for each of the four designated focus areas show different IWV variations on different time scales (Fig. 9). For all regions, a substantial inter-annual to inter-decadal variability is observed. For the ocean regions, IWV relative variations between −11% and +18% (ocean S) to +22% (ocean N) are detected. For the inland regions, even higher variations between −20% (land S) to −24% (land N) and +30% (land S) to +31% (land N) are detected. The absolute numbers of positive and negative deviations and the distribution of the 1-year CMA IWV (Fig. 10) show that wet extremes are less frequent but more pronounced. This means the dry state is closer to the mean condition. A similar effect is generally observed for the ENSO state with El Niño typically showing stronger departures from the mean compared to La Niña. (See Fig. 11.)

The highest peak within the 111-year record occurs for the northern ocean region during the 1997 El Niño. This El Niño yields a peak for all focus regions for the 1-year CMA and is still a prominent feature in the 5-year CMA. Thereafter, IWV has been decreasing in all regions until

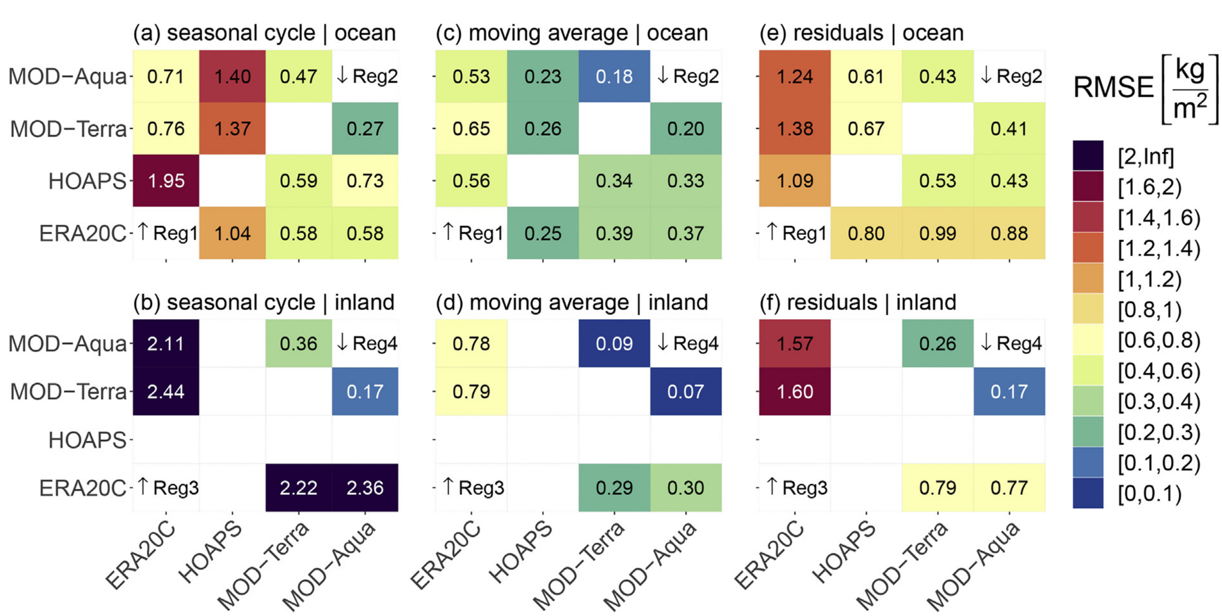

Fig. 6. Same as Fig. 5 but for root mean square error (RMSE).

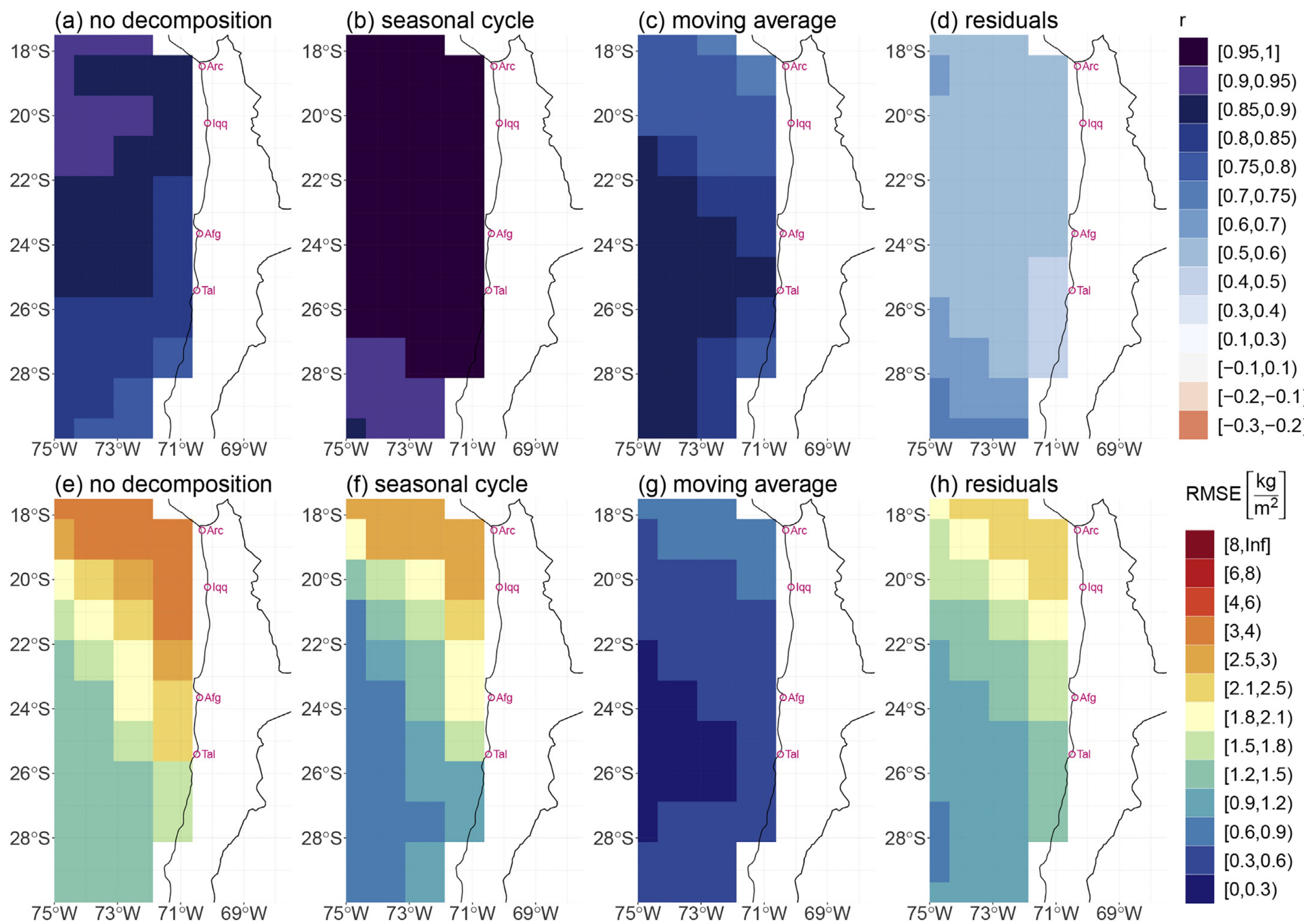

Fig. 7. Spatial distribution of correlation r (a–d), and RMSE (e–h) between HOAPS4 and ERA-20C on a 1.25° × 1.25° grid for a 23-year period (1988–2010). Shown are the parameters for the time series with no decomposition, the seasonal cycle, the moving average, and the residuals (left to right).

the end of the covered period. Therefore, compared to the late 1990s, the years around 2010 constitute a dry period. However, since the 1970s, IWV has been increasing in all four focus regions until the end of the 20th century (Fig. 9c). The latter coincides with a shift from cold to warm phase of the PDO (Fig. 11c) which will be discussed in more detail in Section 4.2.

Correlations between the individual regions (Fig. 12) range around 0.65 to 0.7 for the 1-year CMA indicating rather pronounced coupling between the regions. An exception is the northern inland region which correlates less to the southern inland region (0.58) and the southern ocean region (0.16). This indicates that the northern inland region responds differently to short term variability and is less connected in particular to the southern regions. On the other hand, the northern inland region shows higher correlations on longer time scales (10-year CMA) with the southern ocean region (0.47) and the northern ocean region (0.85). On shorter time scales, periods with more frequent wet episodes might still cause a distinct signal in the 1-year CMA which is smoothed on longer time scales. During summer, such wet episodes can occur in the northeastern Atacama (Altiplano) when easterly winds advect moist air from Amazon basin into the region. These easterlies appear in connection to a southward displacement of the Bolivian High which is a seasonal upper tropospheric high pressure system. It is present during summer with a mean climatological position above Bolivia (Garreaud et al., 2009). The origin of the moisture is the continental boundary layer in central South America. Diurnal heating of the eastern Andean slopes along with entrainment of easterly momentum from upper levels results in strong upslope transport of moisture (Garreaud, 1999; Garreaud et al., 2003). Enhanced summer precipitation (Vuille, 1999) and enhanced summer IWV (Marín and Barrett, 2017) over the Altiplano are associated with this synoptic pattern. While individual wet episodes connected to upper level easterlies typically last for a couple of days up to a week, their frequency of occurrence can vary on inter-annual time scales (Garreaud et al., 2003). Therefore, the moisture variability due the described mechanism could be visible in 1-year CMA of the IWV. However, the described impacts of a southward displacement of the Bolivian High are constraint to the northern part of the Atacama. This could be an explanation why the northern inland focus region might be less connected to the other focus regions, especially the southern regions. A still higher correlation with the northern ocean region could be an indication that the easterly moisture transport might even reach the Pacific. How this phenomenon relates to longer term climate variability (ENSO, PDO) is discussed in Section 4.2 and Section 4.3 with seasonal distinction.

4.2. IWV relationship with ENSO, PDO and local SST

To assess how the described variability of regional IWV in the Atacama and bordering southeast Pacific is connected to larger scale climate variations, we investigate its relationship to ENSO and the PDO. Furthermore, local SST anomalies determined from the ERA-20C SST (Section 2.4) are considered. ENSO, PDO and the local SST are all positively correlated (Fig. 12). This is not surprising since all these indices usually feature warm (cold) SST anomalies in the southeast Pacific during their warm (cold) phase. However, ENSO, PDO and local SST act

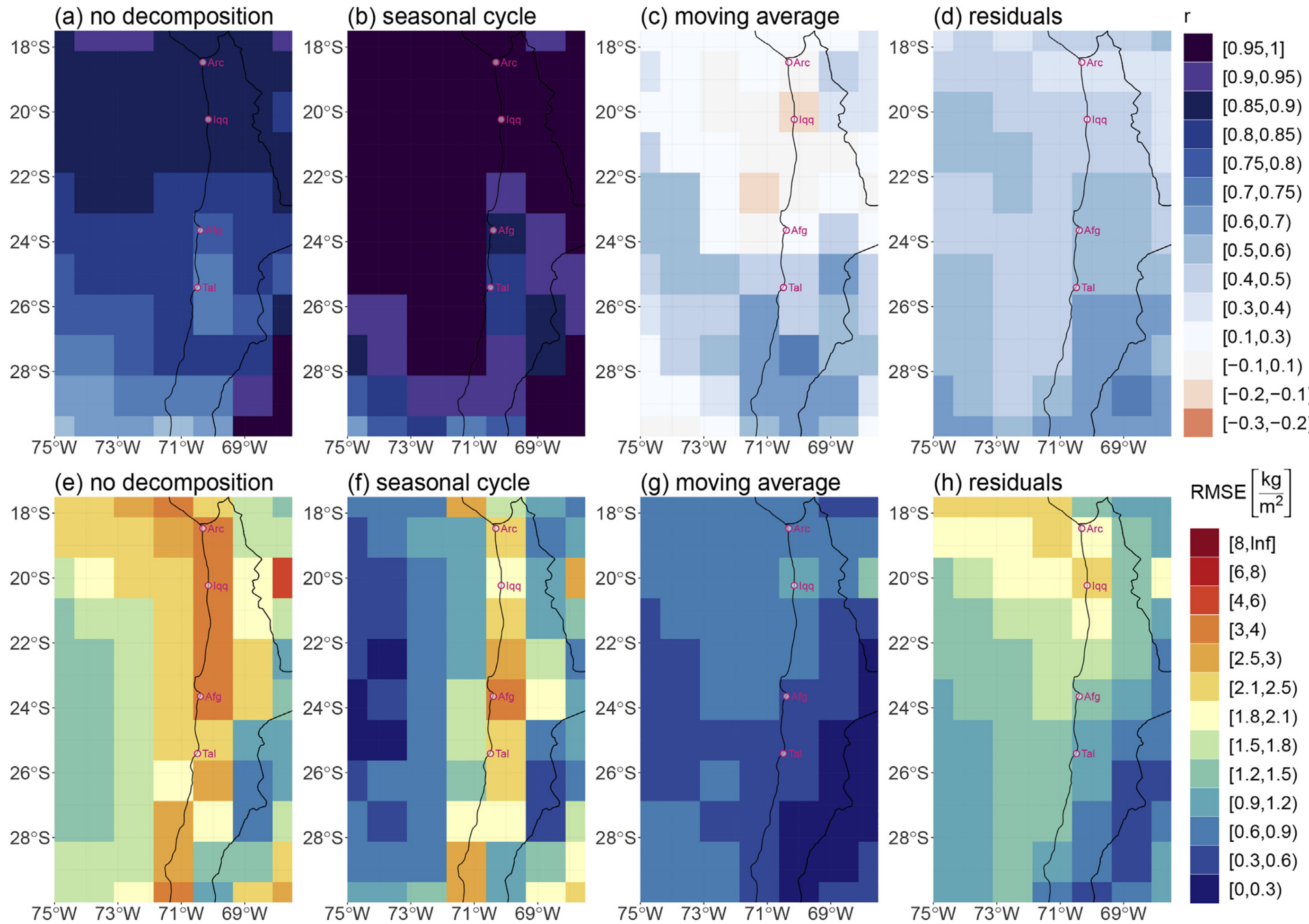

Fig. 8. Spatial distribution of correlation r (a–d), and RMSE (e–h) between Terra-MODIS and ERA-20C on a 1.25 ° × 1.25° grid for a 10-year period (2001–2010). Shown are the parameters for the time series with no decomposition, the seasonal cycle, the moving average, and the residuals (left to right). Here, the IWV from the 15 UTC output of ERA-20C is utilized.

on different time and spatial scales, so that different relationships to the local IWV can be expected. In particular ENSO and PDO feature more pronounced teleconnection patterns compared to local SST. Therefore, a more complex relationship to local IWV can be expected for these two large scale features.

All indices feature mainly positive relationships with the IWV of the focus regions, indicating higher IWV during the respective warm phases. An exception is the northern inland region which does not show a correlation to local SST and PDO ($r \approx 0$), but a slight negative correlation to ENSO ($r = -0.22$) for the 1-year CMA. This means, the region is drier during El Niño and wetter during La Niña. Previous studies have shown this effect for the Altiplano during the austral summer season mainly for precipitation (Vuille, 1999; Garreaud et al., 2003; Canedo-Rosso et al., 2019) but also for specific humidity (Vuille, 1999). During El Niño, which typically reaches its mature state during austral summer, the Bolivian High weakens and retreats to the north, so that pronounced upper level westerlies steer dry air towards the Altiplano (Vuille, 1999). On the contrary, during austral winter an opposite relationship has been reported. Enhanced ridging over the Pacific in higher latitudes and troughing over the southeastern Pacific result in a northward displacement of midlatitude disturbances yielding wetter winters mainly in the southern Atacama (Vargas et al., 2006; Houston, 2006). Extended northward troughing with anomalous northwesterly midtropospheric flow are also related to higher IWV over the Altiplano during austral winter (Marín and Barrett, 2017). Therefore, opposite responses to the same phase of ENSO are expected for summer and winter season. This could explain generally low correlations of ENSO with the inland IWV in particular for the northern inland region. A more detailed analysis of seasonal effects is presented in Section 4.3.

The mechanism causing anticorrelation between IWV and ENSO during austral summer is more pronounced in the northern region. Therefore, the southern regions are not expected to show such strong seasonal dependence of the relationship. This is manifested in higher correlations between IWV and ENSO for the southern regions (Fig. 12). The PDO is expected to have similar impacts in the study area compared to ENSO but with smaller amplitude (Garreaud et al., 2009). Moreover, PDO and ENSO phases can have constructive interference (Andreoli and Kayano, 2005).

Correlations between indices and regional IWV are generally lower for the 1-year CMA compared the 10-year CMA (Fig. 12). In particular the PDO shows stronger correlations on an inter-decadal time scale compared to an inter-annual time scale. ENSO and to a lesser extent the PDO favor certain weather patterns but are not expected to directly cause them. Therefore, not every El Niño is associated with increased precipitation at the southern coast of the Atacama (Houston, 2006) or anomalous dry episodes in the Altiplano (Vuille, 1999; Garreaud et al., 2003). The variability is still related to particular synoptic patterns. For instance, an extreme precipitation event occurred in the Atacama in March 2015 which was associated with an El Niño. Bozkurt et al. (2016) demonstrate that only the interplay of the positive SST anomalies and a concurrent cut-off low enabled the enhanced moisture transport which ultimately fueled the unusual precipitation inland. The

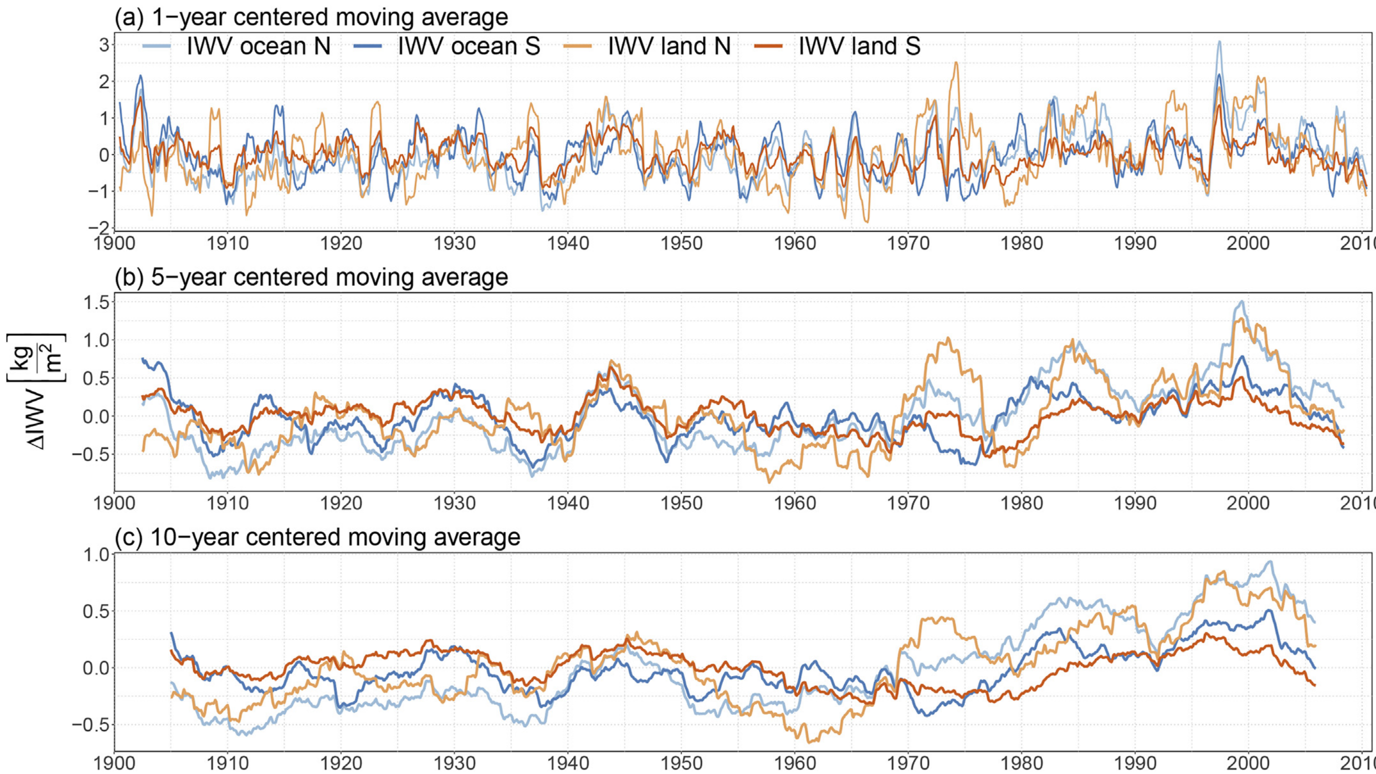

Fig. 9. Time series of IWV anomalies from ERA-20C for the northern and southern ocean and inland regions indicated in Fig. 1. Shown are the 1-year (a), 5-year (b) and 10-year (c) centered moving averages between the years 1900 and 2010.

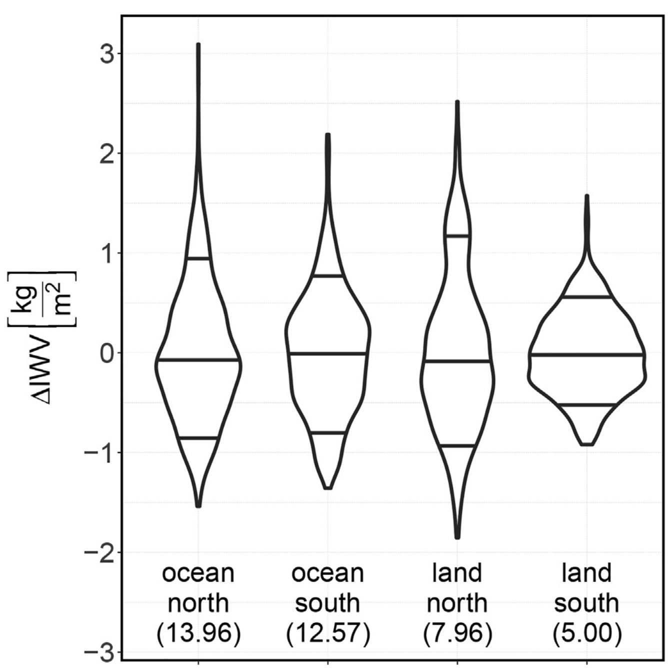

Fig. 10. Violins of IWV anomalies based on monthly values of the 1-year centered moving average (time series shown in Fig. 9a) between 1900 and 2010 for the four focus regions indicated in Fig. 1. Horizontal lines within the violins represent the 10th, 50th and 90th percentile of the distribution. The overall mean value is given in parenthesis for each region in kg m^{-2}.

synoptic variability influences the IWV resulting in lower correlations especially for shorter time scales.

For the southern inland region, the PDO explains more variability compared to ENSO and local SST. This raises the hypothesis that during the warm phase of the PDO the frequency of blocking situations in higher latitudes with an accompanied northward shift of midlatitude disturbances is increased. The latter pattern yields wetter conditions in the Atacama during austral winter. It occurs more often during the developing stage of El Niño (Vargas et al., 2006).

Over ocean and also for the northern inland region, the local SST appears to have the strongest relationship with the IWV on an interdecadal time scale compared to ENSO and PDO. This implies that the direct connection from an increased SST to a higher IWV is stronger than the more complex relationship with ENSO and PDO. An increased SST causes a warming and moistening of the MBL. An increase of the water holding capacity of warmer air by about 7% per Kelvin is expected according to the Clausius-Clapeyron relation so that the IWV would most likely increase for a higher SST.

This direct relationship between local SST and IWV is also manifested by the results of lagged correlations. The highest correlation is yielded for lag 0 (Fig. 13c). ENSO and PDO yield higher correlations if the IWV is shifted back in time by 2–5 months (Fig. 13a and b). This supports the results from Vargas et al. (2006) who reported that the pattern of anomalous ridging over the Pacific in higher latitudes and troughing in subtropical latitudes is favored during the developing stage of El Niño. Therefore, enhanced wetness would be expected a few month prior to the fully developed El Niño.

4.3. Seasonal dependencies

To investigate the seasonal dependence, we calculate the normalized density of the monthly IWV distinguished between austral winter (JJA) and summer (DJF) season for each of the four focus regions. Further, we distinguish between different states of the Niño 3.4 index and the local SST by defining intervals with break points resulting from different quartiles of the respective index (Fig. 14). El Niño like conditions, i.e. the top quartile of the Niño 3.4 index, lead to above average IWV during winter (JJA, Fig. 14 a–d) and decreased IWV variability

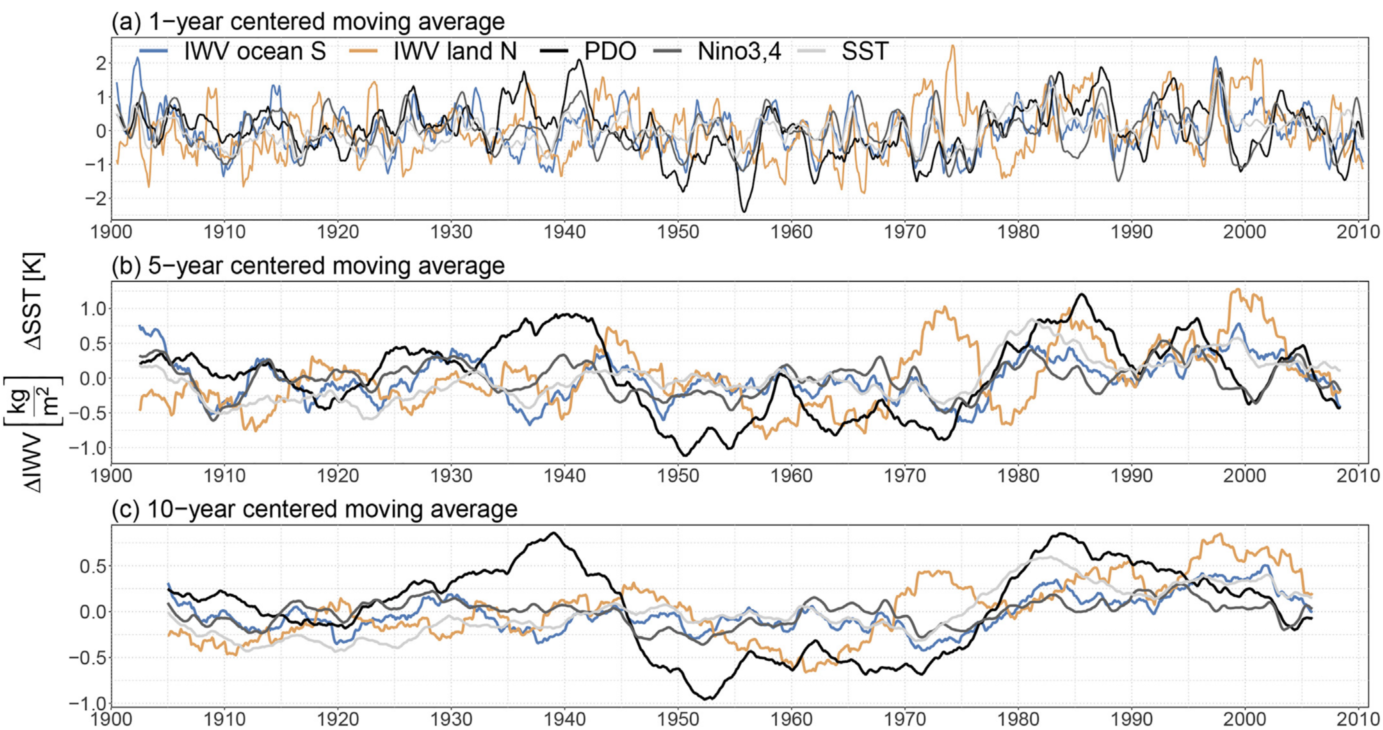

Fig. 11. Same as Fig. 9 but only for the southern ocean and northern inland regions. Additional lines of different shades of gray represent the PDO index, Niño 3,4 index, and the local SST anomalies. Local SST is taken from ERA-20C averaged over the region ranging from 75.625°W to 71.875°W, and from 29.375°S to 18.125°S).

(narrower distribution) during summer (DJF, Fig. 14 e–h) with a shift to the dry end of the overall IWV range. La Niña like conditions, i.e. the lowest quartile of the Niño 3.4 index, lead to below average IWV during winter (JJA, Fig. 14 a–d) and only show a small difference compared to the neutral ENSO state (i.e. interquartile range of the Niño 3.4 index). For the northern inland and ocean region, la Niña allows slightly higher wet extremes of IWV compared to neutral or El Niño conditions during the summer. However, the drier conditions during El Niño are a lot more pronounced. A mechanism behind this could be enhanced upper tropospheric easterly wind flow during La Niña. Vuille (1999) demonstrate that a high southern oscillation index (SOI), which represents La Niña conditions, is associated with a more pronounced and southward shifted Bolivian high which leads to increased easterly winds over the Altiplano. On the other hand, El Niño conditions result in a weakened Bolivian High and stronger westerlies. Garreaud et al. (2003) also show that while enhanced easterlies strengthen the upslope flow of moist continental air on the eastern side of the Andes, weakened easterlies strengthen the upslope flow of dry desert air on the western side of the

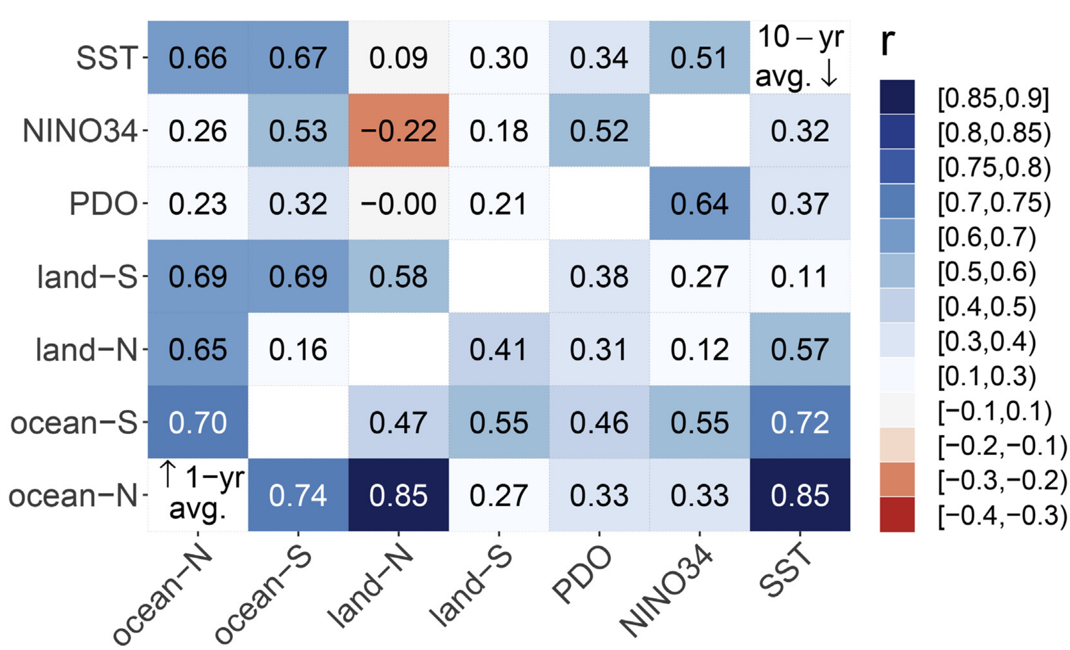

Fig. 12. Correlations between the different time series, namely the ERA-20C IWV for 4 different regions (ocean and inland, north and south as indicated in Fig. 1), PDO index, Niño 3,4 index, and the local SST. Shown are results for a 1-year moving average (upper left) and a 10-year moving average (lower right). Correlation coefficients r are indicated by colour and are given as numbers.

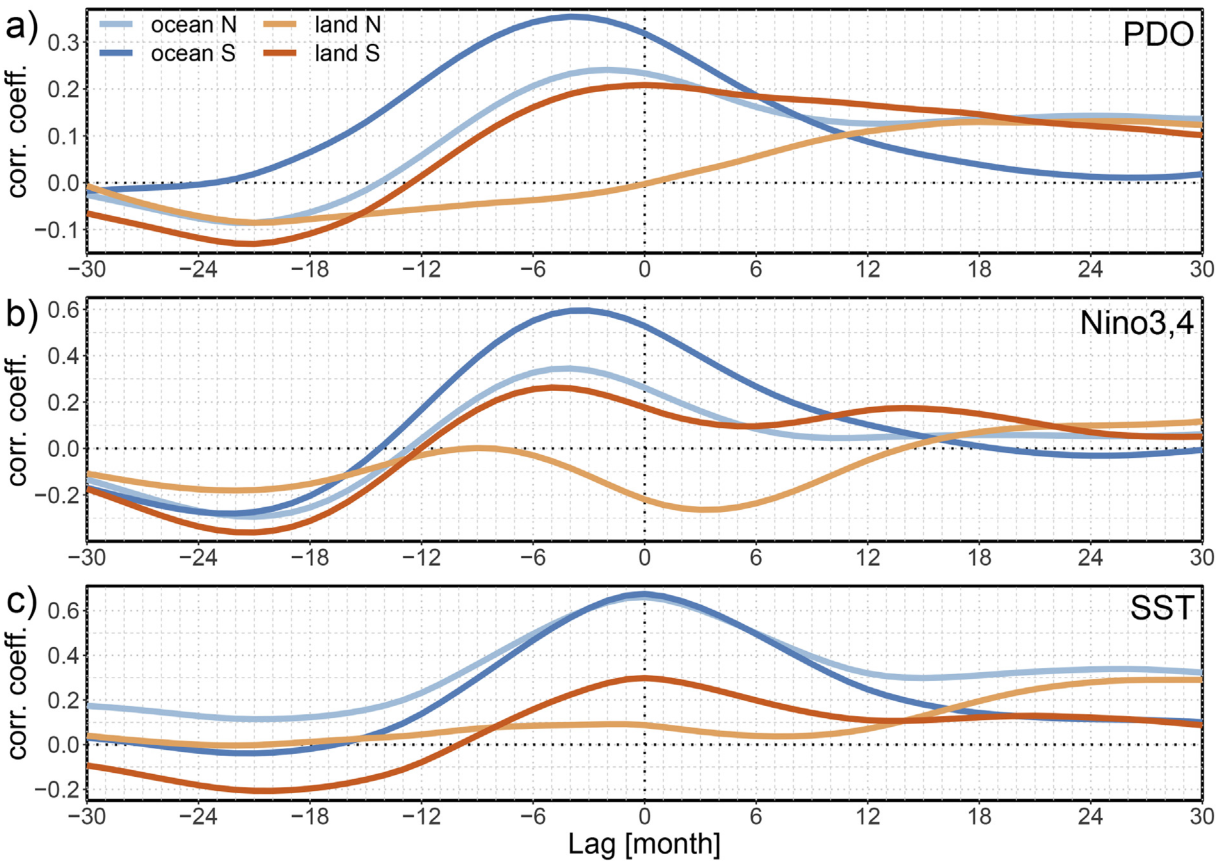

Fig. 13. Correlation coefficients for lagged correlations between ERA-20C IWV and PDO (a), Niño3,4 index (b) and local SST (c) for the 1-year centered moving averages. Distinguished are the 4 focus regions (ocean north, ocean south, land North, land south). The lag k indicates that the correlation is calculated between the time series IWV_{t+k} and the respective index ind_t (PDO, Niño3,4 or local SST).

Andes. La Niña conditions, which are typically associated with intensified subsidence over the eastern Pacific, potentially trigger enhanced easterly airflow over the Altiplano and control the position of the Bolivian high. These moist upper tropospheric easterlies associated with La Niña conditions cause increased specific humidity even at Antofagasta (Vuille, 1999), a coastal city in the Atacama region.

Analogous results have been obtained for precipitation by Houston (2006). He reports that higher winter precipitation in the Atacama occurs during El Niño conditions, whereas enhanced summer precipitation occurs during La Niña conditions. The principle agreement of our findings with the results from Houston (2006) indicates the close relationship between IWV and precipitation. Thus, long term IWV retrievals might link to precipitation estimates for the past.

For the winter season, the effects of the local SST appear similar compared to the effects of the Niño 3.4 index. This means that higher local SSTs correspond to a shift towards higher IWV values whereas lower local SSTs correspond to a shift towards lower IWV values (Fig. 14 i–l). For the summer season, only the ocean regions show a dependence on local SST (Fig. 14 m–p). Moreover, only the upper quartile of the SST range appears to have an effect on the IWV, by shifting the distribution towards higher values.

5. Conclusion

We investigated the IWV within the Atacama Desert and the bordering southeast Pacific over the course of the 20th century. For IWV estimates, we utilized the reanalysis ERA-20C. In order to assess its suitability, we carried out a validation study first by comparing ERA-20C IWV to different satellite observations (HOAPS, MODIS). On a climatological scale, spatial and seasonal patterns are well reproduced by ERA-20C. Furthermore, a dry bias between 2 $kg\,m^{-2}$ to 3 $kg\,m^{-2}$ for the ocean regions and between 4 $kg\,m^{-2}$ and 6.5 $kg\,m^{-2}$ for the inland regions is found, which can be attributed to an underestimation of the MBL and the coarse representation of the topography by ERA-20C. This is in agreement to Poli et al. (2016) who found a similar bias between HOAPS and ERA-20C for spatial averages over the tropical ocean (between 20°S and 20°N). Such biases are not uncommon among reanalyses (Schröder et al., 2017) and do not hinder the representation of variability.

Thus, in order to study the temporal variability of the IWV, we consider anomalies. It is found that even specific synoptic features, i.e. cut-off lows, are represented very well in ERA-20C. Furthermore, a time series analysis for four different focus regions revealed that temporal variability of IWV in ERA-20C is overall in accordance with the satellite observations. In particular, the phase of the seasonal cycle is captured well with correlations reaching almost unity. The inter-annual variability is represented well with correlations between ERA-20C and HOAPS of about 0.82 (ocean north) and 0.89 (ocean south). However, for a short period between 2005 and 2008, the inter-annual variability of ERA-20C IWV deviates about 1 $kg\,m^{-2}$ from HOAPS and MODIS observations. This period of disagreement becomes a dominant feature for the comparison of ERA-20C and MODIS IWV due to the short overlapping time period (2003–2010). A possible reason for the disagreement could be a change in the assimilated observations. However, the seasonal cycle and the month to month variability are still represented well even for this time period.

The validation is carried out for the time past 1988 for which HOAPS data, which constitute the longest record of satellite based IWV observations, are available. As no area wide IWV observations are available prior to the satellite era, we have to rely on reanalyses. A

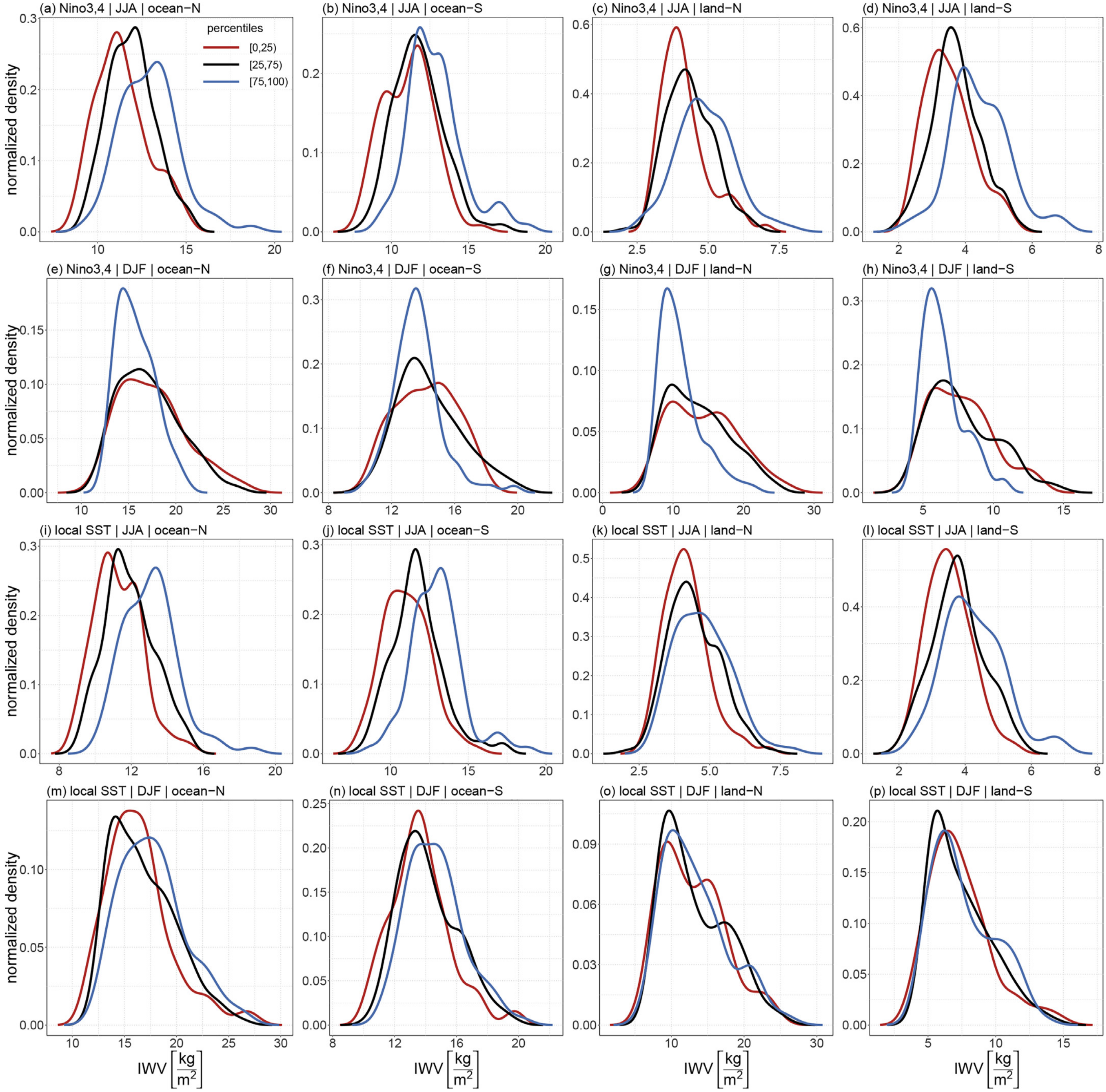

Fig. 14. Composite normalized density of IWV retrieved from ERA-20C for the covered time period (1900–2010) for different conditions of the Niño 3,4 index (a–h) and of the local SST anomaly (i-p). The 4 focus regions are distinguished by 4 columns. Furthermore, winter season (JJA, 1st and 3rd row) and summer season (DJF, 2nd and 4th row) are shown separately. IWV densities are shown for lowest quartile (red), the inter-quartile range (black) and the highest quartile (blue) of the respective indices. This way, the red curves represent conditions typically associated with La Niña like conditions and the blue curve represent conditions typically associated with El Niño like conditions. The analysis is based on monthly values of the indices. (For interpretation of the references to colour in this figure legend, the reader is referred to the web version of this article.)

further assessment of the observation feedback archive for ERA-20C revealed an increased uncertainty for the beginning of the 20th century. However, no systematic biases were identified which would hamper a useful analysis. We could show that ERA-20C is capable of representing IWV variability realistically by only assimilating surface pressure and wind observations along with temporally varying forcing data for the Atacama region.

In the second part of this study, we investigated the IWV variability which is represented in ERA-20C over the course of 111 years (1900–2010). Inter-annual variability is high with deviations of the 12 months running mean from the overall mean rising above 30% for example for the inland regions. Furthermore, varying trends on inter-decadal time scales are observed. For instance, an increase of IWV is detected after 1970 until the strong El Niño in 1997/1998 and a decline thereafter, which is in particular pronounced in the northern regions. This increase is consistent with global warming which increases the water vapor holding capacity. However, between 1979 and 2006 local cooling trends have been found for coastal stations in the Atacama

(Falvey and Garreaud, 2009). Another explanation of the increased IWV during the last quarter of the century could be the PDO which shows a concurrent shift into a positive phase during the 1970s. The onset of this positive trend from the 1970s onward and its potential linkage to the PDO as well as various earlier trends could not be revealed using reanalysis which only cover recent decades, such as ERA-Interim (Dee et al., 2011).

In general, warm phases of PDO, ENSO and local SST are associated with increased IWV, except for the northern inland region. A more detailed picture is revealed when a seasonal distinction is applied. While El Niño typically features a dry austral summer, La Niña allows dry and wet summers. This phenomenon is identified for all regions but most pronounced in the northern regions. While the mechanisms behind dry summers under El Niño conditions have been described mainly for the Altiplano in the northeastern part of the Atacama (e.g. Vuille, 1999; Garreaud et al., 2003), it remains unclear if the same mechanisms, i.e. enhanced westerlies/ suppressed easterlies, explain the observed dry conditions for the southern regions during the warm phase of ENSO. For the austral winter season, El Niño conditions have an opposite effect compared to the summer. Then, increased IWV is associated with the warm ENSO phase, while drier conditions are found for La Niña. We found overall positive correlations between ENSO and regional IWV on inter-annual time scales (Fig. 12). This implies that the increase of IWV during winter is generally stronger than the overall lower IWV during the summer associated with El Niño. This seasonal opposite effects seem more balanced for the northern regions manifested in lower correlations (Fig. 12). An even negative correlation for the northern inland region indicates the following: The drying effect due to enhanced westerlies during El Niño summers overcompensates the increased IWV signal during El Niño winters. This results in overall drier years associated with the warm ENSO phase. However, there might be potential tipping points for very strong El Niño events which might alter the previously described relations. An example could be the 1997/98 El Niño for which the northern ocean region yields the highest peak within the entire ERA-20C record (Fig. 9).

La Niña conditions can feature a wider range of IWV during the summer compared to El Niño. While dry summers are typical during El Niño conditions, they can also occur during La Niña conditions. However, wetter summers are limited to La Niña. This indicates, that while the ENSO state favors certain conditions, the synoptic variability is still an important factor to influence the IWV. This is also evident from the higher correlations between the indices and IWV for the long term moving averages (10-year) when synoptic variability is smoothed out compared to shorter time scales.

Generally, the local SST explains the most variability compared to ENSO and PDO. This might be due to the more complex relationship between ENSO (or PDO) and IWV. The impacts of ENSO depend on region and season. Additionally to an immediate impact on IWV via increased SST according to the ENSO phase, teleconnection patterns change the general circulation patterns over the study region complicating the relation to IWV.

Furthermore, the PDO as well as the Niño 3.4 index and the local SST can only partially explain the IWV variability within the four focus regions. Highest correlations are found between the local SST and the IWV of the ocean regions. Therefore, other features have to be identified which further influence the IWV. This could be different weather types which might in turn be controlled by ENSO to a certain degree. Future studies could further exploit ERA-20C. For instance, it would be interesting to investigate to which degree the circulation in different levels of the troposphere is influencing the regional IWV. Marín and Barrett (2017) found that during fall, winter and spring season, high IWV episodes in the Altiplano are concurrent with intensified troughing to the east of northern Chile. The resulting northwesterly flow advects anomalous humid air to the Altiplano. Their study is based on reanalysis data for more recent decades (1979–2010) which are dominated by PDO warm phase. The long record of ERA-20C would allow to test whether the PDO phase influences the weather patterns which yield lower or higher IWV. Moreover, the relationship between ENSO and IWV could be investigated in dependence on the PDO phase. Andreoli and Kayano (2005) already investigated this relationship with regard to precipitation for the period between 1948 and 1999 for the South-American continent. Their findings reveal more conspicuous El Niño signals during the warm PDO phase with more pronounced seasonal differences.

Clouds and precipitation are much more difficult to simulate compared to water vapor as they result from the interplay of many small scale processes. Only a few station records with partly missing data provide precipitation estimates within the Atacama. Available satellite estimates of precipitation, e.g. the Tropical Rainfall Measuring Mission (TRMM), suffer from uncertainties and biases which are greater than the actual signal for the extreme environment of the Atacama (Schween et al., 2020). Therefore, it would be desirable to potentially use IWV as a proxy for precipitation in order to estimate the amount of liquid water which is provided to the land surface and the biosphere. A regional study in the Spanish Mediterranean area demonstrated that IWV is closely related to extreme precipitation (Priego et al., 2017). To investigate whether IWV can serve as a proxy for precipitation, investigations with cloud resolving models are planned in the future.

Declaration of Competing interests

The authors declare that they have no conflict of interest.

Data Availability

ERA-20C data were downloaded from the ECMWF data server via Web-API. HOAPS data were ordered from the CM-SAF Web User Interface (https://wui.cmsaf.eu/, last access: 16 October 2018). MODIS data were downloaded via MODIS Level 1 Atmosphere Archive and Distribution System (LAADS Web) from https://ladsweb.modaps.eosdis.nasa.gov/archive/allData/61/MOD05_L2/.

Acknowledgements

We thank two anonymous reviewers for their constructive comments on the manuscript. We gratefully acknowledge financial support by the Deutsche Forschungsgemeinschaft (DFG, German Research Foundation) – project number 268236062 – SFB 1211.

Appendix A. Supplementary data

Supplementary data to this article can be found online at https://doi.org/10.1016/j.gloplacha.2020.103192.

References

Andersson, A., Graw, K., Schröder, M., Fennig, K., Liman, J., Bakan, S., Hollmann, R., Klepp, C., 2017a. Hamburg ocean atmosphere parameters and fluxes from satellite data - hoaps 4.0. https://doi.org/10.5676/EUM_SAF_CM/HOAPS/V002.

A. Andersson, K. Graw, M. Schröder, K. Fennig, J. Liman, and Rainer Hollmann. Validation report ssm/i and ssmis products hoaps version 4.0, 2017b. https://doi.org/10.5676/EUM_SAF_CM/HOAPS/V002.

Andreoli, R.V., Kayano, M.T., 2005. Enso-related rainfall anomalies in south america and associated circulation features during warm and cold pacific decadal oscillation regimes. Int. J. Climatol. 250 (15), 2017–2030. https://doi.org/10.1002/joc.1222. https://rmets.onlinelibrary.wiley.com/doi/abs/10.1002/joc.1222.

Böhm, C., Sourdeval, O., Mülmenstädt, J., Quaas, J., Crewell, S., 2019. Cloud base height retrieval from multi-angle satellite data. Atmospheric Measurement Techniques 120 (3), 1841–1860. https://doi.org/10.5194/amt-12-1841-2019. URL. https://www.atmos-meas-tech.net/12/1841/2019/.

Borbas, E., Menzel, P., Gao, B., 2017a. Modis atmosphere l2 water vapor product. In: NASA MODIS Adaptive Processing System, Goddard Space Flight Center, https://doi.org/10.5067/MODIS/MOD05_L2.061.

Borbas, E., Menzel, P., Gao, B., 2017b. Modis atmosphere l2 water vapor product. In: NASA MODIS Adaptive Processing System, Goddard Space Flight Center, https://doi.org/10.5067/MODIS/MYD05_L2.061.

Bozkurt, D., Rondanelli, R., Garreaud, R., Arriagada, A., 2016. Impact of warmer eastern tropical pacific sst on the march 2015 atacama floods. Monthly Weather Rev. 1440 (11), 4441–4460. https://doi.org/10.1175/MWR-D-16-0041.1.

Canedo-Rosso, C., Uvo, C.B., Berndtsson, R., 2019. Precipitation variability and its relation to climate anomalies in the bolivian altiplano. Int. J. Climatol. 390 (4), 2096–2107. https://doi.org/10.1002/joc.5937. URL. https://rmets.onlinelibrary.wiley.com/doi/abs/10.1002/joc.5937.

Cereceda, P., Osses, P., Larrain, H., Salvador, Martn, Lagos, M.M. Faras, Pinto, R., Schemenauer, R.S., 2002. Advective, orographic and radiation fog in the tarapac region, chile. Atmosph. Res. 64, 261–271 09.

Cereceda, P., Larrain, H., Osses, P., FarÃ-as, M., EgaÃ ± a, I., 2008. The spatial and temporal variability of fog and its relation to fog oases in the atacama desert, chile. Atmosph. Res. 870 (3), 312–323. https://doi.org/10.1016/j.atmosres.2007.11.012. ISSN 0169-8095. URL. http://www.sciencedirect.com/science/article/pii/S0169809507002104 Third International Conference on Fog, Fog Collection and Dew.

Cockell, C.S., McKay, C.P., Warren-Rhodes, K., Horneck, G., 2008. Ultraviolet radiation-induced limitation to epilithic microbial growth in arid deserts dosimetric experiments in the hyperarid core of the atacama desert. J. Photochem. Photobiol. B: Biol. 900 (2), 79–87. https://doi.org/10.1016/j.jphotobiol.2007.11.009. ISSN 1011-1344. URL. http://www.sciencedirect.com/science/article/pii/S1011134407001790.

Compo, G.P., Whitaker, J.S., Sardeshmukh, P.D., Matsui, N., Allan, R.J., Yin, X., Gleason, B.E., Vose, R.S., Rutledge, G., Bessemoulin, P., Brönnimann, S., Brunet, M., Crouthamel, R.I., Grant, A.N., Groisman, P.Y., Jones, P.D., Kruk, M.C., Kruger, A.C., Marshall, G.J., Maugeri, M., Mok, H.Y., Nordli, Ã., Ross, T.F., Trigo, R.M., Wang, X.L., Woodruff, S.D., Worley, S.J., 2011. The twentieth century reanalysis project. Quart. J. R. Meteorol. Soc. 1370 (654), 1–28. https://doi.org/10.1002/qj.776. URL. https://rmets.onlinelibrary.wiley.com/doi/abs/10.1002/qj.776.

Cordero, R., Damiani, A., Seckmeyer, G., Jorquera, J., Caballero, M., Rowe, P., Ferrer, J., Mubarak, R., Carrasco, J., Rondanelli, R., Matus, M., Laroze, D., 2016. The solar spectrum in the atacama desert. Scient. Rep. 6, 22457. 3. https://doi.org/10.1038/srep22457.

Dai, A., Wang, J., Thorne, P.W., Parker, D.E., Haimberger, L., Wang, X.L., 2011. A new approach to homogenize daily radiosonde humidity data. J. Climate 240 (4), 965–991. https://doi.org/10.1175/2010JCLI3816.1.

Dee, D.P., Uppala, S.M., Simmons, A.J., Berrisford, P., Poli, P., Kobayashi, S., Andrae, U., Balmaseda, M.A., Balsamo, G., Bauer, P., Bechtold, P., Beljaars, A.C.M., van de Berg, L., Bidlot, J., Bormann, N., Delsol, C., Dragani, R., Fuentes, M., Geer, A.J., Haimberger, L., Healy, S.B., Hersbach, H., Hólm, E.V., Isaksen, L., KÃ¥llberg, P., Köhler, M., Matricardi, M., McNally, A.P., Monge-Sanz, B.M., Morcrette, J.-J., Park, B.-K., Peubey, C., de Rosnay, P., Tavolato, C., Thépaut, J.-N., Vitart, F., 2011. The era-interim reanalysis: configuration and performance of the data assimilation system. Quart. J. R. Meteorol. Soc. 1370 (656), 553–597. https://doi.org/10.1002/qj.828. URL. https://rmets.onlinelibrary.wiley.com/doi/abs/10.1002/qj.828.

Elliott, W.P., Gaffen, D.J., 1991. On the utility of radiosonde humidity archives for climate studies. Bull. Am. Meteorol. Soc. 720 (10), 1507–1520. https://doi.org/10.1175/1520-0477(1991)072<1507:OTUORH>2.0.CO;2.

Falvey, M., Garreaud, R.D., 2009. Regional cooling in a warming world: Recent temperature trends in the southeast pacific and along the west coast of subtropical south america (19792006). J. Geophys. Res. Atmosph. 1140 (D4). https://doi.org/10.1029/2008JD010519. URL. https://agupubs.onlinelibrary.wiley.com/doi/abs/10.1029/2008JD010519.

Farr, T.G., Rosen, P.A., Caro, E., Crippen, R., Duren, R., Hensley, S., Kobrick, M., Paller, M., Rodriguez, E., Roth, L., Seal, D., Shaffer, S., Shimada, J., Umland, J., Werner, M., Oskin, M., Burbank, D., Alsdorf, D., 2007. The shuttle radar topography mission. Rev. Geophys. 450 (2). https://doi.org/10.1029/2005RG000183. URL. https://agupubs.onlinelibrary.wiley.com/doi/abs/10.1029/2005RG000183.

Fennig, K., Andersson, A., Bakan, S., Klepp, C.-P., Schröder, M., 2012. Hamburg ocean atmosphere parameters and fluxes from satellite data - hoaps 3.2 - monthly means/6-hourly composites. https://doi.org/10.5676/EUM_SAF_CM/HOAPS/V001. URL.

Folland, C.K., Parker, D.E., 1995. Correction of instrumental biases in historical sea surface temperature data. Quart. J. R. Meteorol. Soc. 1210 (522), 319–367. https://doi.org/10.1002/qj.49712152206. URL. https://rmets.onlinelibrary.wiley.com/doi/abs/10.1002/qj.49712152206.

C. K. Folland and D. E. Parker. Observed Variations of Sea Surface Temperature, pages 21–52. Springer Netherlands, Dordrecht, 1990. ISBN 978-94-009-2093-4. https://doi.org/10.1007/978-94-009-2093-4_2.

Gao, B.-C., Kaufman, Y.J., 2003. Water vapor retrievals using moderate resolution imaging spectroradiometer (modis) near-infrared channels. J. Geophys. Res. Atmosph. 1080 (D13). https://doi.org/10.1029/2002JD003023. URL. https://agupubs.onlinelibrary.wiley.com/doi/abs/10.1029/2002JD003023.

Garreaud, R.D., 1999. Multiscale analysis of the summertime precipitation over the Central Andes. Monthly Weather Rev. 1270 (5), 901–921. https://doi.org/10.1175/1520-0493(1999)127<0901:MAOTSP>2.0.CO;2.

Garreaud, R., Vuille, M., Clement, A.C., 2003. The climate of the altiplano: Observed current conditions and mechanisms of past changes. Palaeogeogr. Palaeoclimatol. Palaeoecol. 1940 (1–3), 5–22. ISSN 0031-0182. 5. https://doi.org/10.1016/S0031-0182(03)00269-4.

Garreaud, R.D., Vuille, M., Compagnucci, R., Marengo, J., 2009. Present-day south american climate. Palaeogeogr. Palaeoclimatol. Palaeoecol. 2810 (3), 180–195. https://doi.org/10.1016/j.palaeo.2007.10.032. ISSN 0031-0182. URL. http://www.sciencedirect.com/science/article/pii/S0031018208005002 Long-term multi-proxy climate reconstructions and dynamics in South America (LOTRED-SA): State of the art and perspectives.

Hannay, C., Williamson, D.L., Hack, J.J., Kiehl, J.T., Olson, J.G., Klein, S.A., Bretherton, C.S., Köhler, M., 2009. Evaluation of forecasted southeast pacific stratocumulus in the ncar, gfdl, and ecmwf models. J. Clim. 220 (11), 2871–2889. https://doi.org/10.1175/2008JCLI2479.1.

He, J., Liu, Z., Dec 2019. Comparison of satellite-derived precipitable water vapor through near-infrared remote sensing channels. IEEE Trans. Geosci. Remote Sens. 570 (12), 10252–10262. https://doi.org/10.1109/TGRS.2019.2932847. ISSN 1558-0644.

Hersbach, H., Poli, P., Dee, D.P., 2015. The observation feedback archive for the icoads and ispd data sets. In: Technical Report 18. 05 ECMWF, Shinfield Park, Reading URL. https://www.ecmwf.int/node/9871.

Hollinger, J.P., Peirce, J.L., Poe, G.A., Sep. 1990. Ssm/i instrument evaluation. IEEE Trans. Geosci. Remote Sens. 280 (5), 781–790. https://doi.org/10.1109/36.58964. ISSN 0196-2892.

Houston, J., 2006. Variability of precipitation in the atacama desert: Its causes and hydrological impact. Int. J. Climatol. 260 (15), 2181–2198. https://doi.org/10.1002/joc.1359. URL. https://rmets.onlinelibrary.wiley.com/doi/abs/10.1002/joc.1359.

F. Kerber, R. R. Querel, R. Rondanelli, R. Hanuschik, M. van den Ancker, O. Cuevas, A. Smette, J. Smoker, T. Rose, and H. Czekala. An episode of extremely low precipitable water vapour over Paranal observatory. Month. Notices R. Astron. Soc., 4390 (1): 247–255, 02 2014. ISSN 0035-8711. https://doi.org/10.1093/mnras/stt2404.

Khaniani, A.S., Nikraftar, Z., Zakeri, S., 2020. Evaluation of modis near-ir water vapor product over iran using ground-based gps measurements. Atmosph. Res. 231, 104657. https://doi.org/10.1016/j.atmosres.2019.104657. ISSN 0169-8095. URL. http://www.sciencedirect.com/science/article/pii/S0169809519303047.

Laloyaux, P., de Boisseson, E., Balmaseda, M., Bidlot, J.-R., Broennimann, S., Buizza, R., Dalhgren, P., Dee, D., Haimberger, L., Hersbach, H., Kosaka, Y., Martin, M., Poli, P., Rayner, N., Rustemeier, E., Schepers, D., 2018. Cera-20c: A coupled reanalysis of the twentieth century. J. Adv. Model. Earth Syst. 100 (5), 1172–1195. https://doi.org/10.1029/2018MS001273. URL. https://agupubs.onlinelibrary.wiley.com/doi/abs/10.1029/2018MS001273.

Mantua, N.J., Hare, S.R., Zhang, Y., Wallace, J.M., Francis, R.C., 1997. A pacific interdecadal climate oscillation with impacts on salmon production. Bull. Am. Meteorol. Soc. 780 (6), 1069–1080. https://doi.org/10.1175/1520-0477(1997)078<1069:APICOW>2.0.CO;2.

Marín, J.C., Barrett, B.S., 2017. Seasonal and intraseasonal variability of precipitable water vapour in the chajnantor plateau, chile. Int. J. Climatol. 370 (S1), 958–971. https://doi.org/10.1002/joc.5049. URL. https://rmets.onlinelibrary.wiley.com/doi/abs/10.1002/joc.5049.

McHugh, T.A., Morrissey, E., Reed, S., Hungate, B., Schwartz, E., 2015. Water from air: An overlooked source of moisture in arid and semiarid regions. Scient. Rep. 50 (13767), 9. https://doi.org/10.1038/srep13767.

Muñoz, R.C., Zamora, R.A., Rutllant, J.A., 2011. The coastal boundary layer at the eastern margin of the southeast pacific (23.4s, 70.4w): Cloudiness-conditioned climatology. Journal of Climate 240 (4), 1013–1033. https://doi.org/10.1175/2010JCLI3714.1.

Otarola, A., De Breuck, C., Travouillon, T., Matsushita, S., Nyman, L.-Å., Wootten, A., Radford, S.J.E., Sarazin, M., Kerber, F., Pérez-Beaupuits, J.P., Mar 2019. Precipitable water vapor, temperature, and wind statistics at sites suitable for mm and submm wavelength astronomy in northern chile. Publ. Astron. Soc. Pacific 1310 (998), 045001. https://doi.org/10.1088/1538-3873/aafb78.

Pinto, R., Barra, I., Marquet, P.A., 2006. Geographical distribution of tillandsia lomas in the atacama desert, northern chile. J. Arid Environ. 650 (4), 543–552. https://doi.org/10.1016/j.jaridenv.2005.08.015. ISSN 0140-1963. URL. http://www.sciencedirect.com/science/article/pii/S0140196305002193.

Poli, P., Hersbach, H., Dee, D.P., Berrisford, P., Simmons, A.J., Vitart, F., Laloyaux, P., Tan, D.G.H., Peubey, C., Thépaut, J.-N., Tremolet, Y., Hólm, E.V., Bonavita, M., Isaksen, L., Fisher, M., 2016. Era-20c: An atmospheric reanalysis of the twentieth century. J. Clim. 290 (11), 4083–4097. https://doi.org/10.1175/JCLI-D-15-0556.1.

Priego, E., Jones, J., Porres, M.J., Seco, A., 2017. Monitoring water vapour with gnss during a heavy rainfall event in the spanish mediterranean area. Geomat. Nat. Hazards Risk 80 (2), 282–294. https://doi.org/10.1080/19475705.2016.1201150.

Rahn, D.A., Garreaud, R., 2010. Marine boundary layer over the subtropical southeast pacific during vocals-rex part 1: Mean structure and diurnal cycle. Atmosph. Chem. Phys. 100 (10), 4491–4506. https://doi.org/10.5194/acp-10-4491-2010. https://www.atmos-chem-phys.net/10/4491/2010/.

Rayner, N.A., Parker, D.E., Horton, E.B., Folland, C.K., Alexander, L.V., Rowell, D.P., Kent, E.C., Kaplan, A., 2003. Global analyses of sea surface temperature, sea ice, and night marine air temperature since the late nineteenth century. J. Geophys. Res. Atmosph. 1080 (D14). https://doi.org/10.1029/2002JD002670. URL. https://agupubs.onlinelibrary.wiley.com/doi/abs/10.1029/2002JD002670.

Remy, D., Falvey, M., Bonvalot, S., Chlieh, M., Gabalda, G., Froger, J.-L., Legrand, D., 2011. Variability of atmospheric precipitable water in northern chile: Impacts on interpretation of insar data for earthquake modeling. J. South Am. Earth Sci. 310 (2), 214–226. https://doi.org/10.1016/j.jsames.2011.01.003. ISSN 0895-9811. http://www.sciencedirect.com/science/article/pii/S0895981111000046.

Reyers, M., Shao, Y., 2019. Cutoff lows off the coast of the atacama desert under present day conditions and in the last glacial maximum. Global Planet. Change 181, 102983. https://doi.org/10.1016/j.gloplacha.2019.102983. ISSN 0921-8181. URL. http://www.sciencedirect.com/science/article/pii/S0921818119300050.

Rondanelli, R., Molina, A., Falvey, M., 2015. The atacama surface solar maximum. Bull. Am. Meteorol. Soc. 960 (3), 405–418. https://doi.org/10.1175/BAMS-D-13-00175.1.

Rutllant, J.A., Fuenzalida, H., Aceituno, P., 2003. Climate dynamics along the arid northern coast of chile: The 19971998 dinmica del clima de la regin de antofagasta (diclima) experiment. J. Geophys. Res. Atmosph. 1080 (D17). https://doi.org/10.

1029/2002JD003357. ISSN 2156-2202. 4538.
Schröder, M., Lockhoff, M., Forsythe, J.M., Cronk, H.Q., Haar, T.H. Vonder, Bennartz, R., 2016. The gewex water vapor assessment: Results from intercomparison, trend, and homogeneity analysis of total column water vapor. J. Appl. Meteorol. Climatol. 550 (7), 1633–1649. https://doi.org/10.1175/JAMC-D-15-0304.1.
Schröder, M., Lockhoff, M., Shi, L., August, T., Bennartz, R., Borbas, E., Brogniez, H., Calbet, X., Crewell, S., Eikenberg, S., Fell, F., Forsythe, J., Gambacorta, A., Graw, K., Ho, S.-P., Höschen, H., Kinzel, J., Kursinski, E.R., Reale, A., Roman, J., Scott, N., Steinke, S., Sun, B., Trent, T., Walther, A., Willen, U., Yang, Q., November 2017. GEWEX water vapor assessment (G-VAP). In: WCRP report 16/2017. World Climate Research Programme (WCRP), Geneva Switzerland, pp. 216.
Schween, J.H., Hoffmeister, D., Löhnert, U., 2020. Filling the observational gap in the atacama desert with a new network of climate stations. Global Planet. Change 184, 103034. https://doi.org/10.1016/j.gloplacha.2019.103034. ISSN 0921-8181. URL. http://www.sciencedirect.com/science/article/pii/S0921818119305193.
Steinke, S., Eikenberg, S., Löhnert, U., Dick, G., Klocke, D., Di Girolamo, P., Crewell, S., 2015. Assessment of small-scale integrated water vapour variability during hope. Atmosph. Chem. Phys. 150 (5), 2675–2692. https://doi.org/10.5194/acp-15-2675-2015. URL. https://www.atmos-chem-phys.net/15/2675/2015/.
Stevens, B., Bony, S., 2013. Water in the atmosphere. Physics Today 66, 29–34. 06. https://doi.org/10.1063/PT.3.2009.
Surma, J., Assonov, S., Herwartz, D., Voigt, C., Staubwasser, M., 2018. The evolution of 17o-excess in surface water of the arid environment during recharge and evaporation. Scient. Rep. 80 (4972), 1–10. https://doi.org/10.1038/s41598-018-23151-6.
Tang, Y., Gao, J., Liu, C., Chen, X., Zhao, Y., 2019. Dehydration pathways of gypsum and the rehydration mechanism of soluble anhydrite α-caso4. ACS Omega 40 (4), 7636–7642. https://doi.org/10.1021/acsomega.8b03476.
Timmermann, A., An, S.-I., Kug, J.-S., Jin, F.-F., Cai, W., Capotondi, A., Cobb, K., Lengaigne, M., McPhaden, M.J., Stuecker, M.F., Stein, K., Wittenberg, A.T., Yun, K.-S., Bayr, T., Chen, H.-C., Chikamoto, Y., Dewitte, B., Dommenget, D., Grothe, P., Guilyardi, E., Ham, Y.-G., Hayashi, M., Ineson, S., Kang, D., Kim, S., Kim, W.M., Lee, J.-Y., Li, T., Luo, J.-J., McGregor, S., Planton, Y., Power, S., Rashid, H., Ren, H.-L., Santoso, A., Takahashi, K., Todd, A., Wang, G., Wang, G., Xie, R., Yang, W.-H., Yeh, S.-W., Yoon, J., Zeller, E., Zhang, X., July 2018. El niño southern oscillation complexity. Nature 559, 535–545. https://doi.org/10.1038/s41586-018-0252-6.
Vargas, G., Rutllant, J., Ortlieb, L., 2006. Enso tropicalextratropical climate teleconnections and mechanisms for holocene debris flows along the hyperarid coast of western south america (1724s). Earth Planet. Sci. Lett. 2490 (3), 467–483. https://doi.org/10.1016/j.epsl.2006.07.022. ISSN 0012-821X. URL. http://www.sciencedirect.com/science/article/pii/S0012821X06005140.
Vuille, M., 1999. Atmospheric circulation over the bolivian altiplano during dry and wet periods and extreme phases of the southern oscillation. Int. J. Climatol. 190 (14), 1579–1600. https://doi.org/10.1002/(SICI)1097-0088(19991130)19:14<1579::AID-JOC441>3.0.CO;2-N. URL. https://rmets.onlinelibrary.wiley.com/doi/abs/10.1002/.
Wentz, F.J., 2013. Ssm/i version-7 calibration report. URL. http://images.remss.com/papers/rsstech/2012_011012_Wentz_Version-7_SSMI_Calibration.pdf RSS Technical Report 011012.
Wood, R., Mechoso, C.R., Bretherton, C.S., Weller, R.A., Huebert, B., Straneo, F., Albrecht, B.A., Coe, H., Allen, G., Vaughan, G., Daum, P., Fairall, C., Chand, D., Klenner, L. Gallardo, Garreaud, R., Grados, C., Covert, D.S., Bates, T.S., Krejci, R., Russell, L.M., de Szoeke, S., Brewer, A., Yuter, S.E., Springston, S.R., Chaigneau, A., Toniazzo, T., Minnis, P., Palikonda, R., Abel, S.J., Brown, W.O.J., Williams, S., Fochesatto, J., Brioude, J., Bower, K.N., 2011. The vamos ocean-cloud-atmosphere-land study regional experiment (vocals-rex): goals, platforms, and field operations. Atmosph. Chem. Phys. 110 (2), 627–654. https://doi.org/10.5194/acp-11-627-2011. URL. https://www.atmos-chem-phys.net/11/627/2011/.
Wyant, M.C., Wood, R., Bretherton, C.S., Mechoso, C.R., Bacmeister, J., Balmaseda, M.A., Barrett, B., Codron, F., Earnshaw, P., Fast, J., Hannay, C., Kaiser, J.W., Kitagawa, H., Klein, S.A., Köhler, M., Manganello, J., Pan, H.-L., Sun, F., Wang, S., Wang, Y., 2010. The prevoca experiment: modeling the lower troposphere in the southeast pacific. Atmosph. Chem. Phys. 100 (10), 4757–4774. https://doi.org/10.5194/acp-10-4757-2010. URL. https://www.atmos-chem-phys.net/10/4757/2010/.
Zhang, Y., Wallace, J.M., Battisti, D.S., 1997. Enso-like interdecadal variability: 190093. J. Clim. 100 (5), 1004–1020. https://doi.org/10.1175/1520-0442(1997)010<1004:ELIV>2.0.CO;2.